Modeling Ablation in Al/CuO Nanothermite Pellet Combustion

by

Mohsen Mondegari

A thesis
presented to the University of Waterloo
in fulfillment of the
thesis requirement for the degree of
Master of Applied Science
in
Mechanical and Mechatronics Engineering

Waterloo, Ontario, Canada, 2025

© Mohsen Mondegari 2025

Author's Declaration

I hereby declare that I am the sole author of this thesis. This is a true copy of the thesis, including any required final revisions, as accepted by my examiners.

I understand that my thesis may be made electronically available to the public.

Abstract

Nanothermites are reactive materials composed of metal and metal oxide nanoparticles, engineered to produce rapid exothermic reactions with high energy density. Aluminum and copper oxide (Al/CuO) are widely used due to their strong reactivity and ability to achieve efficient combustion, making them ideal for applications in energetic materials.

This thesis investigates the combustion of Al/CuO nanothermite pellets, with a particular focus on ablation—mass loss due to thermal degradation and chemical reactions. A numerical model is developed to capture key combustion characteristics, including flame speed, pressure distribution, and temperature response, while accounting for both thermal and mechanical effects across varying packing densities. Leveraging the Porous-material Analysis Toolbox based on OpenFOAM (PATO), this model simulates complex reactions, heat flux, and ablation dynamics, thereby addressing existing gaps in understanding ablation effects on nanothermite combustion and enhancing predictive capabilities for these materials.

In its simulation methodology, this study adapts PATO to model multiphase reactive materials, formulating governing equations for mass, momentum, and energy conservation. A two-dimensional axisymmetric model was selected to represent the cylindrical pellet structure. Key parameters, including material porosity, permeability, specific heat, and thermal conductivity, were tailored to the properties of nanothermite materials, while distinct boundary conditions were applied to simulate ignition and ablation phases. Simulations were conducted across various packing densities, with some models incorporating ablation-specific boundary conditions to capture changes in flame speed, peak pressure, and pellet stability under different conditions.

Results indicate that ablation intensity significantly influences the combustion dynamics, with higher intensities leading to reduced flame speeds and peak pressures. The study's findings highlight the potential for controlled nanothermite combustion by optimizing pellet packing density and ablation characteristics, offering applications in propulsion and micro-energetics.

Acknowledgments

I would like to express my appreciation for the invaluable guidance, support, and expertise provided by my supervisor, Dr. Jean-Pierre Hickey, throughout the journey of completing this thesis. Additionally, I want to extend my sincere gratitude to Dr. John Wen and all my fellow researchers in the Multi-Physics Interaction Lab (MPI-LAB) and the Laboratory for Emerging Energy Research (LEER). Their insights and discussions have greatly enriched my research experience.

I also want to thank my parents for always believing in me and supporting me to reach this point, and my wife for her enduring sacrifices and encouragements.

Dedication

To my beloved wife, Sima, whose presence in my life makes every challenge easier, every achievement more joyful, and every moment more meaningful.

Table of Contents

Author's Declaration ii

Abstract iii

Acknowledgments iv

Dedication v

List of Figures ix

List of Tables xi

List of Abbreviations xii

List of Symbols xiii

1 Introduction 1

1.1 Background 1

1.2 Motivation and Objectives 4

1.3 Scope of the Thesis 5

1.4 Contributions 6
1.5 Structure of the Thesis 7

2 Literature Review **8**
2.1 Experimental Studies 9
2.2 Numerical Studies 13

3 Simulation Methodology **17**
3.1 Overview of PATO 18
3.2 Generic Model 19
3.2.1 Governing Equations 21
3.2.2 Bprime Boundary Condition 24
3.3 Applications 27
3.3.1 Biomass Pyrolysis 27
3.3.2 Ablative Materials 28

4 Proposed Model **31**
4.1 Conceptual Framework 31
4.2 Simulation Details 33
4.2.1 Model Parameters 33
4.2.2 Geometry, Boundary, and Initial Conditions 37
4.2.3 Grid, Solvers, and Discretization Schemes 39
4.3 Validation 41

5 Results and Discussion **45**

5.1 Baseline Simulation Scenarios 45

5.2 Parameter Sensitivity 54

6 Conclusion **60**

References **63**

APPENDICES **71**

A Detailed Analysis of the Bprime Boundary Condition **72**

List of Figures

2.1 Burning structures at the propagation front of a nanothermite film loaded on a microscope glass [25] 10

2.2 Schematic of the zero-dimensional thermite model: (a) initial system, (b) system during combustion [48] 14

3.1 Architecture and workflow of PATO [26] 19

3.2 Schematic of representative element volume in reactive porous material . . 20

3.3 Schematic of conservation of element mass fraction at the boundary 25

3.4 Schematic of energy balance at the boundary 26

3.5 Modeling levels of different phenomena in porous carbon/phenolic ablative materials [30] 29

4.1 Solid/gas framework of thermite combustion model 32

4.2 Schematic of 2D axisymmetric pellet geometry: a) front view, b) top view . 37

4.3 Coarse examples of computational grid for each scenario 40

4.4 Reproduction of Epps *et al.* [14] results of average flame speed in PATO . 42

4.5 Mesh sensitivity study on flame peak pressure for 10% TMD pellet 43

5.1 Effect of pellet packing density on ignition delay 46

5.2 Temperature and pressure evolution at probes 1 and 3 for 10% TMD pellet (2D scenario without ablation) 47
5.3 Local flame speed with respect to distance from top boundary 49
5.4 Effect of pellet packing density on average flame speed and peak pressure . 50
5.5 Evolution of temperature and pressure contours for 10% TMD pellet (2D scenario without ablation) 51
5.6 Evolution of temperature and pressure contours for 10% TMD pellet (1D scenario with ablation) 52
5.7 Temperature contours at $t = 0.15$ ms for 10% TMD pellet with varying ablation intensity 55
5.8 Effect of ablation intensity on average flame speed and peak pressure . . . 55
5.9 Effect of thermal conductivity on average flame speed 57
5.10 Effect of permeability/viscosity ratio on flame peak pressure 59

List of Tables

1.1 Thermophysical properties of various thermite reactions [17] 3

4.1 Imposed values of ignition delay and exit mass flux for top boundary conditions 39

5.1 Updated values of ignition delay and exit mass flux for sensitivity analysis of thermal conductivity 56

5.2 Results of average flame speed for different K/μ ratios 58

List of Abbreviations

CFD computational fluid dynamics 17

MEMS micro-electromechanical systems 3

NASA National Aeronautics and Space Administration 17

NEMs nanoenergetic materials 2

NIST National Institute of Standards and Technology 34

PATO Porous-material Analysis Toolbox based on OpenFOAM 17–19, 21–24, 26–28, 30, 31, 33, 36, 41, 42, 45, 60, 73

TMD theoretical maximum density 32, 34–36, 40, 43, 44, 46–49, 51, 54

List of Symbols

$\mathcal{A}_i$ Arrhenius law pre-exponential factor of phase i 22

B' Dimensionless mass flow rate 26

C_H Stanton number for heat transfer 25, 26

C_M Stanton number for mass transfer 26

Co Courant number 41

$\mathcal{E}_i$ Arrhenius law activation energy of phase i, J/mol 22

$\mathcal{F}_i$ Diffusion flux of element/species i, kg/m^{2}s 23

F_i Fraction of solid mass lost through pyrolysis reaction of phase i 21

$\underline{\underline{K}}$ Permeability tensor, m^2 23, 35

$\mathcal{M}_i$ Molecular weight of species i, kg/mol 23

$\mathcal{M}$ Mean molecular weight of gas phase, kg/mol 23

N_g Number of gaseous species/elements 19

N_p Number of solid phases 19

Ω_h Overall heterogeneous mass reaction rate, kg/m^{3}s 22

Π Pyrolysis gas production rate, kg/m^{3}s 22

$\mathcal{R}$ Perfect gas constant, J/mol.K 22

$\dot{S}$ Energy production/consumption per volume unit, W/m^3 24, 36

T Temperature, K 22

β Klinkenberg factor, Pa 23

c_p Specific heat capacity at constant pressure, J/kg.K 34

c_v Specific heat capacity at constant volume, J/kg.K 34

χ_i Advancement of pyrolysis reaction of phase i 21

d_c Characteristic pore size, m 35

Δt Time step, s 41

e_t Total energy density, J/kg 24

ϵ Volume fraction 20

h Enthalpy, J/kg 24, 34

k_k Kozeny constant 35

$\underline{\underline{k}}$ Thermal conductivity tensor, J/m^{2}s.K 24, 35

λ Scaling factor 26

$\dot{m}$ Mass flux, kg/m^{2}s 25

m_i Arrhenius law parameter of phase i 22

$\mathcal{K}_i$ Equilibrium constant related to the formation reaction of species A_i 72

μ Gas viscosity, Pa.s 23

n_i Arrhenius law parameter of phase i 22

ω_i^h Effective heterogeneous mass reaction rate of phase i, kg/m^{3}s 21

ω_i Reaction production rate of species i, mol/m^{3}s 23

ϕ Porosity 32, 35

π_i Pyrolysis production rate of species/element i, kg/m^{3}s 23

p Pressure, Pa 23

ρ Density, kg/m^{-3} 20

σ Stefan-Boltzmann constant, W/m^{2}K^4 26

$\mathbf{v_g}$ Convection gas velocity vector, m/s 22

ε Emissivity 26

x_i Species/element mole fraction 72

$\mathbf{x}$ Coordinate vector, m 22

y_i Species mass fraction 22

z_i Element mass fraction 22, 25

Chapter 1

Introduction

1.1 Background

Combustion processes are fundamental to a wide range of industrial and technological applications, forming the foundation of energy generation systems, propulsion technologies, and various manufacturing processes. Recent research has increasingly focused on enhancing the efficiency and performance of these systems while reducing environmental impact through zero-carbon cycles. Metal fuels have emerged as a promising alternative energy carriers in this context, offering high energy density and the ability to release energy through oxidation without producing carbon emissions. This oxidation often yields solid metal oxides as by-products, which in certain cases can be collected and recycled via electrolysis powered by renewable energy, enabling a sustainable, closed-loop energy cycle [5, 19].

Aluminum is a prominent choice among metal fuels for energy release, delivering approximately 31 kJ/g when reacting with oxygen, and is further favored for its abundance and cost-effectiveness compared to alternatives such as boron, silicon, and magnesium [44]. Aluminum particles are extensively used in applications such as propellants, explosives, igniters, and pyrotechnics [10, 43, 52]. A typical form of aluminum used as a fuel is in

thermite reactions, where it reacts with metal oxides as the reducing agent to generate intense heat. Common oxidizers paired with aluminum include cupric oxide (CuO), bismuth trioxide (Bi_2O_3), ferric oxide (Fe_2O_3), and molybdenum trioxide (MoO_3) [16].

Nanothermites, a class of nanoenergetic materials (NEMs), are gaining significant attention for their enhanced combustion properties due to the integration of metal fuels, such as aluminum, with oxidizing agents at the nanoscale. The term 'nanothermites' refers to the nanoscale dimensions of the constituent particles and the resulting structural features that influence their reactivity. Specifically, the metal fuel and oxidizer are often synthesized or arranged with particle sizes in the range of 10–100 nanometers. The use of such nanoscale components provides a larger surface area, enabling faster reaction rates and overcoming the heat and mass transfer limitations typically observed in larger-scale composites. This increased surface interaction allows for tailored combustion properties, offering both high energy density and rapid energy output. Moreover, self-assembly techniques used in nanothermites improve the contact between the metal fuel and oxidizer, enhancing overall reaction efficiency and stability. Despite their high reactivity, advancements in material design have sought to reduce sensitivity to stimuli such as electrostatic discharge and impact, ensuring safer handling and application [45].

Al/CuO nanothermites are particularly notable among Al-based nanothermites due to their exceptional reactivity and energy output. Table 1.1 lists the thermophysical properties of conventional thermites, showing that Al/CuO thermite exhibits a higher energy density on a volumetric basis [17]. The combustion of Al/CuO nanothermites is a self-sustaining exothermic reaction once ignited, involving a complex series of physical and chemical phenomena. Physically, the process includes the melting of aluminum, diffusion of reactants, and expansion of products. Chemically, it involves the reduction of CuO by Al, leading to the formation of alumina (Al_2O_3) and copper (Cu), along with a substantial release of heat. The interaction between these physical and chemical processes governs combustion characteristics such as flame speed, temperature distribution, and the nature of the residues [8].

Table 1.1: Thermophysical properties of various thermite reactions [17]

Reactants	Density [g/cm^3]	Adiabatic Reaction Temperature [K]		Heat of Reaction	
		w/o phase changes	w/ phase changes	[kJ/g]	[kJ/cm^3]
$2\,Al + 3\,CuO$	5.109	5718	2843	4.076	20.82
$2\,Al + Fe_2O_3$	4.175	4382	3135	3.956	16.51
$2\,Al + MoO_3$	3.808	5574	3253	4.703	17.90
$2\,Al + Bi_2O_3$	7.188	3995	3253	2.118	15.22

Interest in Al/CuO nanothermites extends beyond their high energy density; their adaptability for specific applications makes them particularly valuable. Adjustments in composition, particle size, and morphology enable precise control over reaction rate, ignition temperature, and energy release, facilitating material customization for various uses. These applications range from micro-initiators and joining techniques in micro-electromechanical systems (MEMS), to propellants and pyrotechnics in larger-scale systems [2, 11, 21]. Furthermore, diverse structural configurations, including core-shell, physically mixed powders, bilayer nanolaminates, and nanowires, enable nanothermites to exhibit distinct behaviors, broadening their range of applications [12, 33, 40, 58].

Despite their potential, the practical application of Al/CuO nanothermites is limited by challenges in understanding and controlling their combustion behavior. The nanoscale nature of the reactants introduces several complexities, including heightened sensitivity to mechanical, thermal, or electrical stimuli, which may lead to accidental ignition from minimal external disturbances. Additionally, the agglomeration of nanoparticles can reduce overall combustion efficiency, while the rapid and sometimes unpredictable behavior of nanoscale reactions poses challenges for achieving controlled ignition and sustained combustion [20, 33, 54].

Ablation in nanothermite combustion is a critical process characterized by the progressive removal of material from the surface of the reacting system. This phenomenon occurs

either due to intense heat and rapid chemical reactions induced by environmental factors, such as a laser, or through the abrupt ejection of condensed-phase combustion residuals driven by the high pressure gradient between the flame front and the surrounding environment, as demonstrated in experimental studies showing significant surface mass loss. This process plays a pivotal role in influencing combustion efficiency, energy release, and overall material performance [40]. Understanding the mechanisms underlying ablation provides a potential pathway for enhancing the performance and adaptability of nanothermite formulations in applications such as propulsion systems and energetic devices.

Numerical modeling serves as a powerful tool in this context, providing insight into the complex dynamics of nanothermite combustion, which are often challenging to capture experimentally. Simulations allow researchers to investigate the effects of various parameters on the combustion process, predict performance characteristics, and identify optimal conditions for different applications. This approach not only complements experimental findings but also provides a foundation for the design and development of safer and more effective nanothermite systems.

Ultimately, the combustion of Al/CuO nanothermite pellets presents a rich area of study filled with opportunities and challenges. As this thesis progresses, substantial effort is dedicated to developing a numerical model aimed at predicting key characteristics of nanothermite combustion, including reaction dynamics, thermal behavior, and gas flow patterns, thereby providing a framework for anticipating performance and optimizing material properties.

1.2 Motivation and Objectives

The combustion of nanothermite pellets involves complex interactions among heat generation, mechanical properties, and material behavior, all of which significantly influence their overall performance. The effects of laser-induced ablation have been studied through experimental [38, 40] and numerical approaches [37], offering valuable insights into mate-

rial removal mechanisms under intense energy input. However, residual ablation in nanothermites has not been examined as an independent phenomenon. This limitation arises primarily because residual ablation is closely coupled with the combustion process, making its experimental isolation highly challenging. Similarly, numerical models of flame propagation in nanothermites have ignored the impact of mass loss due to residual ablation, focusing instead on broader combustion dynamics [14]. Consequently, the specific role of residual ablation in influencing energy release, flame structure, and combustion efficiency remains poorly understood, highlighting the need for focused research in this domain.

This research aims to develop a comprehensive model for residual ablation in Al/CuO nanothermite pellet combustion, incorporating both thermal and mechanical responses of the material throughout the combustion process. The model is designed to predict temperature distribution, heat flux, and material loss, accounting for the dynamic properties of the nanothermite across different packing densities. By achieving this, the study seeks to enhance understanding of Al/CuO nanothermite combustion dynamics and support the development of more efficient and reliable energetic materials.

By addressing the current gap in understanding the ablation mechanisms in these materials, this research aims to improve predictive capabilities for their performance in real-world applications. The outcomes of this study are expected to facilitate the optimization of nanothermite formulations, enhance the safety and stability of devices utilizing these materials, and support their implementation in future energy and propulsion systems.

1.3 Scope of the Thesis

The scope of the work encompasses the following key aspects:

- A comprehensive review of existing studies on nanothermites, focusing on Al/CuO-based systems, is conducted to identify gaps in current understanding of combustion mechanisms, ablation phenomena, and relevant modeling approaches.

- The governing equations necessary to describe the physical and chemical processes relevant to nanothermite combustion, such as mass conservation, energy conservation, and reaction kinetics, are examined. This includes multi-phase and multi-species formulations to accurately represent thermal and mass transport within the reactive material.

- An open-source library of OpenFOAM is explored to evaluate its suitability for implementing the proposed model, ensuring compatibility with the complex physical processes involved in nanothermite combustion.

- The numerical model configurations are implemented in the selected numerical tool, with careful attention to the accurate representation of the governing equations and boundary conditions.

- The validity of the model is assessed by comparing it against findings from earlier studies, and various scenarios are simulated to investigate the effects of ablation on the combustion characteristics, including flame propagation speed and material loss.

- The results are thoroughly discussed, highlighting the insights gained from the simulations, and the contributions of this study to the field are examined in terms of advancing the understanding of nanothermite combustion and ablation mechanisms.

1.4 Contributions

The novelty of this study lies in the application of an ablation model to nanothermite combustion, providing a comprehensive investigation of flame propagation dynamics with a focus on the role of ablation during the combustion stage. The study is the first to explicitly simulate the combined thermal and mechanical effects of ablation on flame speed and pressure evolution, addressing significant gaps in the understanding of these phenomena. Utilizing a well-established open-source code designed for porous media, the simula-

tions were configured to replicate the specific conditions of thermite combustion, including temperature-dependent material properties, gas-phase reactions, and phase transitions.

This work advances prior research by integrating an innovative approach to model pellet shrinkage and substantial mass loss during combustion, leveraging ablation models previously validated in aerospace and thermal protection contexts. Additionally, the systematic exploration of different packing densities offers valuable insights into optimizing nanothermite performance for various applications. Collectively, these contributions establish a robust foundation for future experimental and numerical studies on nanothermite systems and reactive materials.

1.5 Structure of the Thesis

The remainder of this thesis is structured as follows: Chapter 2 reviews the relevant literature on nanothermites, Al/CuO systems, experimental setups, and the numerical modeling techniques employed in the field. Chapter 3 outlines the methodology employed in this research, describing the governing equations, and its applications. Chapter 4 provides a detailed explanation of the proposed model and its implementation for the nanothermite combustion case. Chapter 5 presents the results and analysis of the combustion behavior of Al/CuO nanothermite pellets, focusing on various parameters and their impact on performance. Chapter 6 provides a summary of the thesis, its contributions, and conclusions drawn from the research. Through this study, we aim to advance our understanding of Al/CuO nanothermites by employing numerical tools to model the complex dynamics of combustion.

Chapter 2

Literature Review

Research on the field of nanothermite combustion is rapidly evolving, situated at the intersection of materials science, chemistry, and physics. This literature delves into both experimental and numerical studies to offer a comprehensive understanding of the combustion mechanisms, reactivity, and performance characteristics of nanothermites, particularly focusing on Al/CuO thermites. The experimental section of this literature review highlights advancements in observation techniques, the role of reactive sintering and laser ablation, and the impact of structural parameters on combustion behavior. In contrast, the numerical studies section explains the development of sophisticated models that predict the dynamics of thermite reactions, emphasizing the influence of particle size, stoichiometry, and reaction kinetics. Additionally, it covers ablation models used in other applications, as well as in nanothermites, to address gaps in the current research. Together, these studies provide a detailed insight into the multifaceted nature of nanothermite combustion, bridging the gap between theoretical predictions and empirical findings.

2.1 Experimental Studies

Experimental studies have been instrumental in uncovering the intricate behaviors of nanothermites during combustion and ablation. These investigations employ advanced techniques to observe reaction dynamics at micro and nanoscales, offering a detailed understanding of how structural parameters, ignition conditions, and heat transfer mechanisms influence performance. By analyzing factors such as flame propagation, reactive sintering, ablation phenomena, and combustion front dynamics, experimental research sheds light on the physical and chemical processes driving nanothermite reactions. This section highlights key experimental contributions, focusing on methodologies and findings that have advanced the understanding of Al/CuO nanothermites, enabling their optimization for controlled energetic applications.

Direct observation of reaction propagation through the use of high-speed microscopy and thermometry represents an advancement in understanding the combustion performance of nanothermites. Wang *et al.* [50] introduce a high-resolution technique that bridges the gap between real-time reaction monitoring and spatial resolution, enabling the visualization of the microscale reaction dynamics of Al/CuO nanocomposite thermites. The experiments reveal a reaction front thickness of approximately 30 μm and temperatures exceeding 3000 K (above the theoretical adiabatic flame temperature of 2843 K [17]), highlighting a thermal gradient over 10^7 K/m. This study underscores the importance of reactive sintering in the combustion process by rapidly melting and coalescing aggregated metal nanoparticles, thereby affecting the initial size of reacting composite powders and, ultimately, the burn times.

In a more recent study, Kim *et al.* [25] focus on the intricate burning structures and propagation mechanisms of nanothermites, specifically examining Al/CuO nanothermite films. The research uncovers the micro to sub-millimeter scale dynamics of combustion, identifying two distinct propagation modes of the combustion front: normal and tangential, with speeds of the order of 10 cm/s and 50 cm/s, respectively. Active burning sites, characterized by reactive sintering, and pre-ignition sites, where materials await sufficient

energy to ignite, play pivotal roles in the combustion process (Figure 2.1). This detailed analysis highlights the complex interplay between reactive sintering and heat transfer in determining the propagation behavior of nanothermites, offering new insights into their combustion mechanisms and potential for controlled energetic reactions.

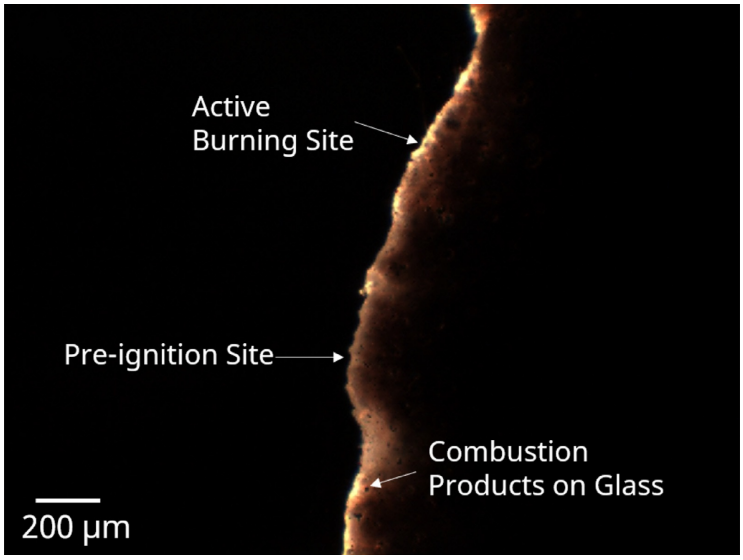


Figure 2.1: Burning structures at the propagation front of a nanothermite film loaded on a microscope glass [25]

Research on nanolaminates, which are thermite films consisting of alternating thin layers (ranging from tens to hundreds of nanometers in thickness) of metals and oxidizers, is also of interest in the field. Bahrami *et al.* [3] explore the synthesis and properties of Al/CuO nanolaminates using DC reactive magnetron sputtering. These nanolaminates are characterized by their tailored stoichiometry and bilayer thickness, allowing precise control over their reactivity and thermal properties. The study reveals that the reactivity and burning rate of these nanolaminates can be significantly influenced by their structural parameters, with thinner bilayers demonstrating faster reaction rates and higher energy release, and a bilayer thickness of 150 nm is identified as the optimal configuration for achieving the best performance.

In another study, Egan *et al.* [12] investigate the ignition behavior of Al/CuO reactive nanolaminates using a temperature jump (T-Jump) technique, which rapidly heats the materials to observe their reaction dynamics under conditions simulating real-world applications. This research confirms the same effect of thinner bilayers on reactivity by reducing ignition temperatures. It also demonstrates that the reactive properties of the nanolaminates can be simulated using a diffusion-based model, suggesting that ignition and reaction rates are heavily influenced by the bilayer interface structure.

Zapata *et al.* [57] focus on the complex Al/CuO self-propagating reaction, characterized by intricate multi-phase and multi-species dynamics, to explore the exceptionally high flame temperatures that reach the vaporization point of alumina, even in a neutral setting. Through experiments using optical spectroscopy and high-speed camera observations on various sputter-deposited Al/CuO multilayers, evidence of AlO and Al in the gas phase indicated that the oxidation-reduction reaction initiates within the bulk nanolaminate. This reaction then quickly separates from the substrate and continues to burn in a mixed phase of condensed and gas in the surrounding environment. The findings showed that the flame temperature is influenced by the stoichiometry but remains unaffected by the bilayer thickness. Furthermore, the research underscored, for the first time, the significant impact of process-induced residual stress, which can cause the multilayer to disrupt prematurely, well before the redox reaction concludes.

Kim and Deng [24] outline a novel framework for inferring chemical kinetics and thermodynamic properties from constant-volume combustion tests of energetic materials. This framework addresses the limitations of traditional performance metrics (ignition delay time, pressurization rate, and maximum pressure) by incorporating a kinetic modeling approach that uses pressure profiles to estimate kinetic and thermodynamic properties. Through a combination of physical and inverse modeling, enhanced by sensitivity analysis, the framework accurately predicts system behaviors during combustion. This innovative approach allows for a more comprehensive understanding of energetic materials' behaviors, offering a method to compare performances across different experimental conditions and laboratories.

The investigations underscore laser ablation as a pivotal process significantly influencing the ignition behavior of nanothermites. Puszynski *et al.* [38] examine the ignition behavior of nanothermites, specifically Al/Fe_2O_3 mixtures, with a focus on factors affecting reaction kinetics and ignition delays. Through laser-pulse exposure experiments, the study demonstrates how porosity, density, and thermal properties influence ignition delay, highlighting that increased porosity reduces delays by lowering thermal conductivity and heat capacity. Additionally, the research evaluates electrostatic discharge (ESD) sensitivity, revealing that particle size, morphology, and the specific heat capacities of fuel and oxidizer significantly impact ignition. These findings emphasize the importance of processing methods and material consolidation in optimizing nanothermites for applications such as primers, electric matches, and low-energy ignition devices.

Similarly, Saceleanu *et al.* [40] explore the combustion and ablation characteristics of physically mixed Al/CuO nanothermites under laser ignition. Using high-speed imaging, the study observes that rapid laser heating causes substantial material ablation, facilitating ignition at the pellet's edge, followed by sustained combustion. Their findings indicate that ablation and flame speed vary significantly with packing density: loosely packed powders exhibit faster propagation driven by mass convection, while denser pellets rely on heat conduction, resulting in slower flame speeds. The work concludes that both the mixture's density and homogeneity are crucial for optimizing ablation and combustion performance, especially as ablation effects enhance surface temperature and promote ignition by reducing heat losses near the ignition site.

Despite the substantial progress in experimental studies on nanothermites, investigations specifically addressing ablation phenomena remain scarce, particularly in the context of their practical applications. To bridge this gap, this section compiles a diverse array of studies related to nanothermites, aiming to illuminate the breadth of research conducted in the field. By exploring key findings on factors such as flame propagation, reactive sintering, thermal properties, and laser ablation, this compilation provides insights into the critical parameters that influence nanothermite behavior and offers guidance for future research priorities in optimizing their performance for energetic applications.

2.2 Numerical Studies

Numerical studies advance the understanding of nanothermite combustion and ablation by modeling reaction kinetics, energy transport, flame propagation, and material decomposition across scales. From zero-dimensional to multi-dimensional simulations, these models explore critical factors like particle size, stoichiometry, and phase transitions, with recent efforts extending to ablation in nanothermites and aerospace applications. This review highlights key contributions, focusing on combustion modeling, flame propagation, and ablation analysis.

In the exploration of zero-dimensional models for nanothermite combustion, Baijot *et al.* [4] present a detailed multi-phase micro-kinetic model for simulating aluminum-based thermite reactions, adopting a hierarchical multiscale approach to predict key combustion parameters—temperature, pressure, and species generation—when Al and CuO nanoparticles react. By integrating atomistic mechanisms such as diffusion, phase transformation, and gas-phase reactions, this model achieves high accuracy with minimal computational cost. The study underscores how parameters like particle size, compaction density, alumina shell thickness, and stoichiometry critically shape combustion dynamics, with experimental results supporting its findings.

Building on this approach, Tichtchenko *et al.* [48] provide a theoretical perspective on Al/CuO thermite combustion within a closed bomb setup, emphasizing the effects of particle size and stoichiometry (Figure 2.2). Using a zero-dimensional model that includes both condensed and gas-phase reactions, they reveal that nanothermites burn approximately ten times faster than microthermites due to enhanced surface area effects, which accelerate oxygen uptake and condensed-phase reactions. Stoichiometry further influences pressure outcomes, as Al-lean mixtures produce higher final pressures through residual gaseous oxygen post-combustion.

Expanding on their earlier work, Tichtchenko *et al.* [47] introduce an advanced triphasic combustion model for Al/CuO thermites, incorporating explicit kinetics across con-

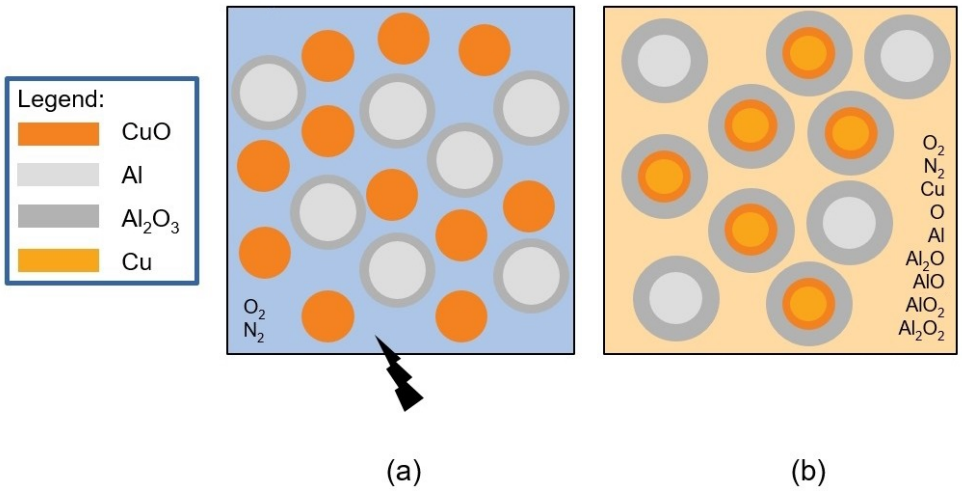


Figure 2.2: Schematic of the zero-dimensional thermite model: (a) initial system, (b) system during combustion [48]

densed and gas phases. This model, characterized by nine gaseous and four condensed species along with 12 heterogeneous reactions and two phase transitions, applies diffusional kinetics and chemical equilibrium to gas-phase reactions. Closed-bomb simulations using this model reveal the pivotal role of Al particle size in pressure dynamics, with smaller particles fostering faster reactions and greater pressure peaks. Together, these studies provide a comprehensive framework for understanding the intricacies of nanothermite combustion, particularly the interplay of particle size, stoichiometry, and reaction kinetics across different combustion phases.

The initial efforts to model flame propagation in nanothermites provide critical insights into their combustion dynamics. Tichtchenko *et al.* [46] developed a two-dimensional, non-stationary model to simulate the combustion of Al/CuO thermite systems, with a focus on n-Al/CuO bilayer thin films. This model incorporates oxygen and aluminum diffusion, enabling detailed analysis of reaction fronts and the effects of bilayer structure, substrate thermal conductivity, and metallic impurities on flame propagation. The study identifies conduction and diffusion as the primary energy transport mechanisms, constrained by

a maximum temperature determined by the copper vaporization point. This limitation reflects the material disintegration caused by pressure and phase changes at elevated temperatures, excluding energy transport from disintegrated particles to the intact thermite.

Similarly, Epps *et al.* [14] proposed a continuum-scale model to investigate flame propagation in laser-ignited porous Al/CuO nanothermite pellets. Their model combines porous media transport with simplified chemical kinetics to simulate combustion dynamics, highlighting the roles of conduction and advection in controlling burn rates. Validated against experimental data, the model provides a detailed sensitivity analysis to identify key parameters influencing combustion regimes.

In the field of heat and mass transfer ablation modeling, Ewing *et al.* [15] present a novel numerical approach to simulating one-dimensional ablation phenomena, with a focus on heat transfer, material decomposition, pyrolysis gas transport, and surface erosion. Their model employs a control-volume-based method with a variable grid, accommodating complex processes such as material swelling and mechanical erosion. The study enables transient thermal analysis of pyrolysis and thermochemical erosion in planar, cylindrical, or spherical geometries, with its accuracy verified through analytical solutions and code comparisons. By integrating features like surface recession and spallation, this work advances ablation modeling, making it applicable to aerospace and thermal protection systems.

Complementing previous work, Mansour *et al.* [31] provide a detailed review of the fluid and thermal dynamics in ablative heat shields, commonly used in aerospace applications. It examines the role of ablation in thermal protection, focusing on how heat flux, material decomposition, and gas flow interact to remove material and dissipate energy. The study emphasizes modeling approaches for predicting ablation under various conditions, providing insights essential for designing efficient thermal protection systems in high-temperature, high-stress environments.

Extending the study of ablation to nanothermites, Peng *et al.* [37] develop a hot-spot model to examine the ablation dynamics of Al/nitrocellulose (NC) nanothermites excited by laser pulses. The model simulates heat diffusion and exothermic chemical reactions,

finding that nanosecond laser pulses drive thermal decomposition, while shorter pulses (e.g., 100 ps) likely induce shock pressure, leading to ablation. The study confirms an ablation criterion where the reacted area expands until it reaches the average interparticle spacing, with the threshold for ablation influenced by factors like pulse duration and nanoparticle size.

In summary, the literature on nanothermite combustion has advanced through experimental and numerical studies, offering detailed insights into reaction dynamics, flame propagation, and material behavior under varying conditions. However, a critical gap remains in the application of ablation models to nanothermite combustion, particularly in examining how residual ablation influence flame propagation speed and combustion characteristics. While existing studies provide robust frameworks for modeling ablation in laser induction and thermal protection contexts, their adaptation to the unique energetic and reactive properties of nanothermites has yet to be fully realized. This study aims to improve an existing flame propagation model by tailoring the ablation model developed in thermal protection contexts to account for residual ablation in nanothermites, thereby capturing their unique energetic and reactive properties more accurately. Addressing this gap could offer a more comprehensive understanding of the interplay between ablation, heat transfer, and reaction mechanisms in nanothermites, paving the way for enhanced control and optimization of their energetic performance.

Chapter 3

Simulation Methodology

In this chapter, the methodology used for conducting the simulations in this study is provided. The Porous-material Analysis Toolbox based on OpenFOAM (PATO) [28], distributed open-source[1] by the National Aeronautics and Space Administration (NASA), was employed to develop and execute the simulations. PATO is an advanced computational tool designed to analyze and simulate the behavior of reactive porous materials. It can be applied to basic heat transfer problems or extended to incorporate advanced functionalities such as internal decomposition (pyrolysis, vaporization), chemical interactions among gases and solids (combustion, cracking, coking), gas species transport (convection, diffusion), and changes in solid morphology (internal density variations, surface ablation) [26]. PATO is implemented as a top-level C++ module within the open-source computational fluid dynamics (CFD) software OpenFOAM[2], integrated with an open-source thermodynamics, transport, and chemistry library Mutation^{++} [41] developed by the von Karman Institute for Fluid Dynamics.

[1] https://software.nasa.gov/software/ARC-16680-1A

[2] https://openfoam.org/

3.1 Overview of PATO

PATO integrates multiple components to handle intricate physical phenomena, specifically tailored to address the complexities associated with porous materials. These materials have unique properties and behaviors that can significantly affect fluid flow, heat transfer, and chemical reactions. PATO extends the functionality of OpenFOAM to model these phenomena more efficiently, providing a powerful toolkit for:

- Multiphase flow simulations
- Heat transfer analysis
- Chemical reaction modeling
- Structural analysis
- Optimization of porous structures

PATO consists of two primary types of modules: global analysis modules and elementary analysis modules. The global analysis modules are used to run comprehensive simulations of reactive porous material responses at a macroscopic scale. The elementary analysis modules focus on detailed microscopic scale phenomena, such as the oxidation of carbon fibers, and are crucial for validating volume-averaged models used in the global analysis modules.

One of the main advantages of PATO is its flexibility and extensibility. It allows researchers to easily implement and test new models, compare different mathematical frameworks, and analyze specific configurations and conditions that may not be readily available in production codes. This makes PATO an excellent platform for both academic research and practical applications.

Its architecture allows for comprehensive input management, including model selection, boundary conditions, material properties, and initial data fields, facilitated by tools like

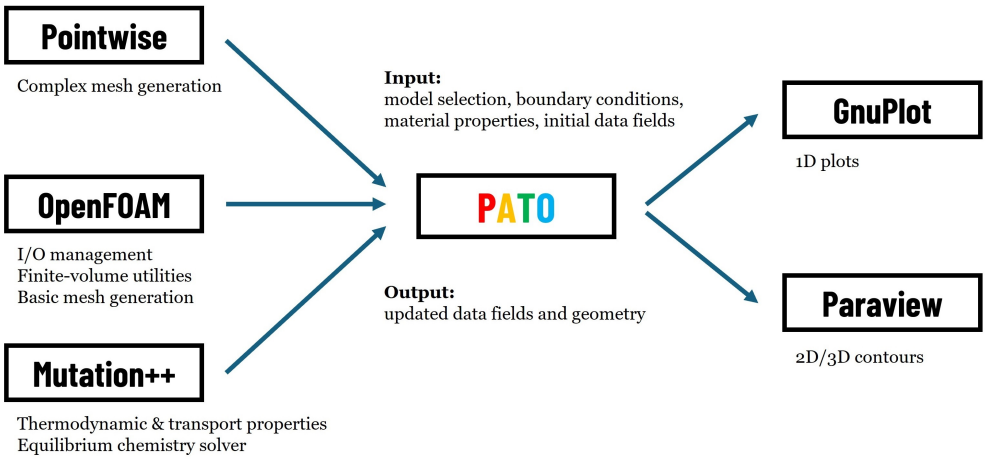


Figure 3.1: Architecture and workflow of PATO [26]

Pointwise for complex mesh generation and Mutation^{++} for thermodynamic and transport properties. The core functionalities of PATO enable simulations ranging from basic Fourier heat transfer to intricate processes such as internal decomposition, gas-solid chemical reactions, gas species transport, and changes in solid morphology. Outputs from PATO, including updated data fields and geometry, are visualized using GnuPlot for 1D plots and Paraview for 2D/3D contours. This integration of advanced modules and visualization tools within PATO's architecture ensures robust and detailed analysis of high-temperature reactive porous materials (Figure 3.1).

3.2 Generic Model

The generic model of PATO is based on several key assumptions regarding the behavior and interactions of multi-phase reactive materials and multi-species reactive gas mixtures. Firstly, it assumes the presence of multiple solid phases (N_p) and various gaseous species/elements (N_g) in one phase, which together form the multi-phase reactive material (Figure 3.2). The core of PATO lies in its ability to handle complex, multi-scale phenom-

ena by using volume-averaged forms of conservation equations for gas mass, gas species, solid mass, gas momentum, and energy in porous media. A fundamental assumption of the model is local thermal equilibrium, implying that all phases are at the same temperature locally. Each solid phase within the material has the potential to undergo pyrolysis, vaporization, or sublimation, thereby releasing species into the gas phase. Furthermore, these solid phases can react with the gas phase, such as through the oxidation of a carbon phase. The gas phase chemistry is modeled to accommodate different scenarios: it can be in chemical equilibrium, follow a finite-rate mechanism, or be frozen, depending on the specific conditions and reactions being considered. These hypotheses provide a comprehensive framework for simulating and analyzing the complex behaviors and interactions within reactive porous materials [27, 28, 29, 30].

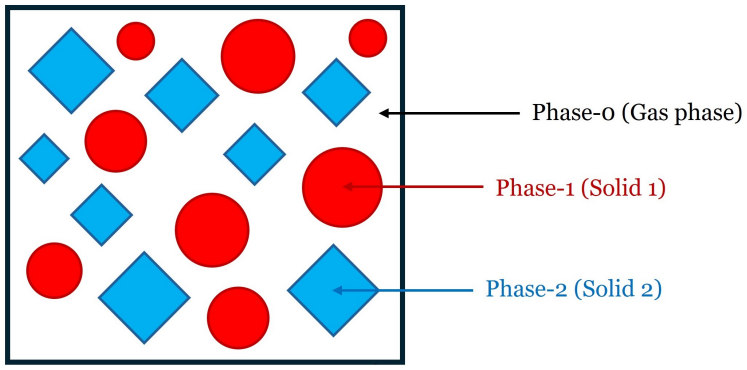


Figure 3.2: Schematic of representative element volume in reactive porous material

Given the solid-gas structure of the model, averaged effective properties are employed for each computational cell to accurately represent the local thermophysical behavior. For instance, density (ρ) can be calculated using the following equation:

$$\rho = \epsilon_g \rho_g + \sum_{i=1}^{N_p} \epsilon_i \rho_i \tag{3.1}$$

where ρ_g and ρ_i represent the intrinsic densities of gas phase and i^{th} solid phase, respectively, and ϵ denotes the volume fractions of each phase. This rule also applies to porosity,

heat capacity, and enthalpy. However, it does not extend to permeability and conductivity, for which we employ linear interpolation between measured values. Notably, the volume fraction of gas phase satisfies the following condition:

$$\epsilon_g = 1 - \sum_{i=1}^{N_p} \epsilon_i \tag{3.2}$$

3.2.1 Governing Equations

The fundamental conservation equations employed in PATO are outlined below. This foundation offers a versatile framework that can be adapted, simplified, or extended to meet the specific demands of diverse applications.

The generic model resolves transport equations in porous media to simulate the flow of heat, mass, and momentum through interconnected voids. The interaction between the solid and gas phases is governed by mass and energy transfer processes occurring between these phases, primarily through pyrolysis, which is the thermal decomposition of materials in the absence of oxygen. This process is complemented by heterogeneous reactions taking place at the gas-solid interface, as well as by phase changes that further influence the system dynamics [29]. For each solid phase, the mass evolution is obtained by the following equation:

$$-\partial_t \left(\epsilon_i \rho_i\right) = \epsilon_{i,0} \rho_{i,0} F_i \partial_t \chi_i + \omega_i^h \tag{3.3}$$

where F_i is the fraction of solid mass lost through pyrolysis reaction, χ_i is the advancement of pyrolysis reaction varying between 0 and 1, and ω_i^h is the heterogeneous mass reaction rate of phase i. The variables with zero subscripts are about the initial values at $t = 0$.

The decomposition of solid phases through pyrolysis is governed by the general form of the Arrhenius law [39],

$$\frac{\partial_t \chi_i}{\left(1 - \chi_i\right)^{m_i}} = T^{n_i} \mathcal{A}_i \exp\left(-\frac{\mathcal{E}_i}{\mathcal{R} T}\right) \tag{3.4}$$

where $\mathcal{E}_i$, $\mathcal{A}_i$, m_i, and n_i are Arrhenius parameters that define the kinetics of the reaction process, $\mathcal{R}$ is perfect gas constant, and T is temperature. There is also the option to include multiple sub-phases with different reaction kinetics for the decomposition of each solid phase. Details on the calculation of heterogeneous mass reaction rates, which are not the focus of this study, are provided in the referenced paper [29].

The conservation of mass for gas phase includes two source terms Π and Ω_h that represent overall pyrolysis gas production rate and heterogeneous mass reaction rate, respectively,

$$\partial_t \left(\epsilon_g \rho_g\right) + \partial_{\mathbf{x}} \cdot \left(\epsilon_g \rho_g \mathbf{v_g}\right) = \Pi + \Omega_h \tag{3.5}$$

where $\mathbf{x}$ and $\mathbf{v_g}$ are coordinate vector (x, y, z) and convection gas velocity vector (u_g, v_g, w_g), respectively. The source terms are obtained as the summation of mass decline in solid phases:

$$\Pi = \sum_{i=1}^{N_p} \epsilon_{i,0} \rho_{i,0} F_i \partial_t \chi_i \tag{3.6}$$

$$\Omega_h = \sum_{i=1}^{N_p} \omega_i^h \tag{3.7}$$

There are three options for the gas-phase chemistry model in PATO: constant elemental composition of pyrolysis gases, detailed equilibrium chemistry, or finite-rate chemistry. In the constant elemental composition model, gas thermodynamic properties can either be tabulated over various ranges of pressure and temperature or computed using the Mutation^{++} library. For equilibrium chemistry assumption, the conservation of element mass fractions (z_i) should be applied:

$$\partial_t \left(\epsilon_g \rho_g z_i\right) + \partial_{\mathbf{x}} \cdot \left(\epsilon_g \rho_g z_i \mathbf{v_g}\right) + \partial_{\mathbf{x}} \cdot \mathcal{F}_i = \pi_i \tag{3.8}$$

The gas species composition is directly calculated based on the local elemental composition, temperature, and pressure using Gibbs minimization technique [42]. For finite-rate chemistry assumption, the conservation of species mass fractions (y_i) should be applied:

$$\partial_t \left(\epsilon_g \rho_g y_i\right) + \partial_{\mathbf{x}} \cdot \left(\epsilon_g \rho_g y_i \mathbf{v_g}\right) + \partial_{\mathbf{x}} \cdot \mathcal{F}_i = \pi_i + \epsilon_g \omega_i \mathcal{M}_i \tag{3.9}$$

In both equations, $\mathcal{F}_i$ and π_i are diffusion flux and pyrolysis production rate of i^{th} element/species, respectively. ω_i is reaction production rate of i^{th} species and $\mathcal{M}_i$ is its molecular weight. Details on equilibrium and finite-rate chemistry models are beyond the scope of this study and are provided in the referenced paper [29].

The conservation of momentum in porous media is governed by Darcy's law with Klinkenberg correction [55],

$$\mathbf{v_g} = -\frac{1+\beta/p}{\epsilon_g \mu}\underline{\underline{K}} \cdot \partial_{\mathbf{x}} p \tag{3.10}$$

where $\underline{\underline{K}}$ is second order tensor of permeability for anisotropic solids, β is Klinkenberg factor, μ is gas viscosity, and p is pressure. The pressure gradient drives the produced gas through the pores at a Darcian flow velocity. The Klinkenberg correction term $(1+\beta/p)$ accounts for slip effects at the pore scale when the Knudsen number (the ratio of the mean free path to the mean pore diameter) is not significantly less than 1. Additional corrections, such as Forchheimer's correction [28], can also be applied or substituted into the momentum equation, depending on the specific application of PATO.

Applying Darcian flow velocity into equation 3.5 with ideal gas assumption for gas phase will result in:

$$\partial_t \left(\frac{\epsilon_g \mathcal{M}}{\mathcal{R}T} p \right) - \partial_{\mathbf{x}} \cdot \left(\frac{p\mathcal{M}}{\mathcal{R}T} \left(\frac{1+\beta/p}{\mu} \underline{\underline{K}} \right) \cdot \partial_{\mathbf{x}} p \right) = \Pi + \Omega_h \tag{3.11}$$

where $\mathcal{M}$ is mean molecular weight of gas phase. Directly solving this equation in terms of pressure, a commonly available boundary condition, offers several advantages over addressing Equations 3.5 and 3.10 separately along with the ideal gas law. However, the non-linear nature of Equation 3.11 with respect to pressure requires careful consideration during discretization. In this approach, the pressure is solved iteratively at each time step, with the factor accompanying the pressure gradient in the non-linear term being updated based on the pressure from the preceding iteration, until convergence is achieved.

Assuming local thermal equilibrium, the energy conservation equation can be expressed as follows, accounting for temporal energy evolution, convection, diffusion, conduction,

viscous dissipation, and source terms:

$$\partial_t \left(\rho_t e_t\right) + \partial_{\mathbf{x}} \cdot \left(\epsilon_g \rho_g h_g \mathbf{v_g}\right) + \partial_{\mathbf{x}} \cdot \sum_{i=1}^{N_g} \left(h_i \mathcal{F}_i\right) = \partial_{\mathbf{x}} \cdot \left(\underline{\underline{k}} \cdot \partial_{\mathbf{x}} T\right) + \mu \epsilon_g^2 \left(\underline{\underline{K}}^{-1} \cdot \mathbf{v_g}\right) \cdot \mathbf{v_g} + \dot{S} \quad (3.12)$$

where h is enthalpy, $\underline{\underline{k}}$ is thermal conductivity tensor, and $\dot{S}$ represents energy production/consumption per unit volume due to pyrolysis or heterogeneous reaction. Total energy density of porous medium (e_t) is calculated by the summation of the energy of its phases:

$$\rho_t e_t = \epsilon_g \rho_g \left(h_g - p/\rho_g\right) + \sum_{i=1}^{N_p} \epsilon_i \rho_i h_i \quad (3.13)$$

The energy conservation equation can be rearranged to isolate energy storage in solid phases and effective heat conduction on one side, while implicitly solving for temperature by treating the remaining terms as explicit source terms. PATO also provides the capability to model scenarios where the solid and gas phases have distinct temperatures, allowing for the definition of a heat transfer coefficient to address energy transfer between them.

In summary, the governing equations presented provide a comprehensive framework for modeling the physical and chemical processes occurring within the system. These equations account for mass, momentum, and energy conservation, as well as the necessary assumptions to capture the complexity of the interactions between different phases. In section 4.2, the application of these equations to nanothermite combustion modeling will be discussed in detail.

3.2.2 Bprime Boundary Condition

In ablative applications of PATO, the surface mass and energy balances are used as boundary conditions, as both the wall temperature and surface recession are unknown. Figure 3.3 presents a schematic representation of the mass fluxes entering and exiting the boundary control volume. Integrating the pyrolysis, transport, and mass equations within the material response framework provides the pyrolysis gas flow rate. However, char ablation

rate depends on pyrolysis gas blowing rate and composition, temperature, pressure, and boundary layer gas composition.

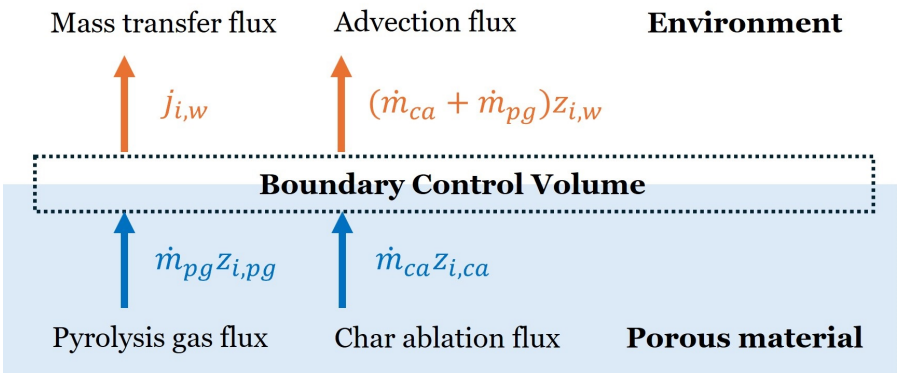


Figure 3.3: Schematic of conservation of element mass fraction at the boundary

Applying element conservation to a steady-state control volume near the boundary, and assuming quasi-steady chemical equilibrium within the control volume, allows for solving the problem [9]. The mass fraction conservation for element i (z_i) within the control volume can be expressed as:

$$j_{i,w} + (\dot{m}_{pg} + \dot{m}_{ca})z_{i,w} = \dot{m}_{pg}z_{i,pg} + \dot{m}_{ca}z_{i,ca} \tag{3.14}$$

where $\dot{m}$ is mass flux and the indices 'pg', 'ca', 'w', and 'e' denote values corresponding to pyrolysis gas, char ablation, the wall, and the environment, respectively. Assuming the Prandtl and Lewis numbers are equal to one and that diffusion coefficients are the same for all elements, the equation $j_{i,w} = \rho_e u_e C_H (z_{i,w} - z_{i,e})$ provides the mass transfer flux, where C_H is the Stanton number. The only unknowns in Equation 3.14 are $z_{i,w}$ and $\dot{m}_{ca}$, which can be determined using chemical equilibrium formulations in Mutation^{++} library within the control volume, given the conditions of p_w and T_w [28]. The quasi-steady assumption implies that variations in p_w, T_w, $\dot{m}_{pg}$, and $\dot{m}_{ca}$ over time are neglected in order to decouple the material response and the boundary layer. The details of chemical equilibrium formulations are discussed in Appendix A.

The material mass loss rate due to char ablation results in a surface ablation velocity given by

$$\mathbf{v}_{ca} = \frac{\dot{m}_{ca}}{\rho_{ca}}\mathbf{n} \tag{3.15}$$

and is applied as a mesh motion in PATO.

The boundary temperature (T_w) can be obtained by applying energy balance on the control volume as depicted in Figure 3.4. The following equation summarizes the conser-

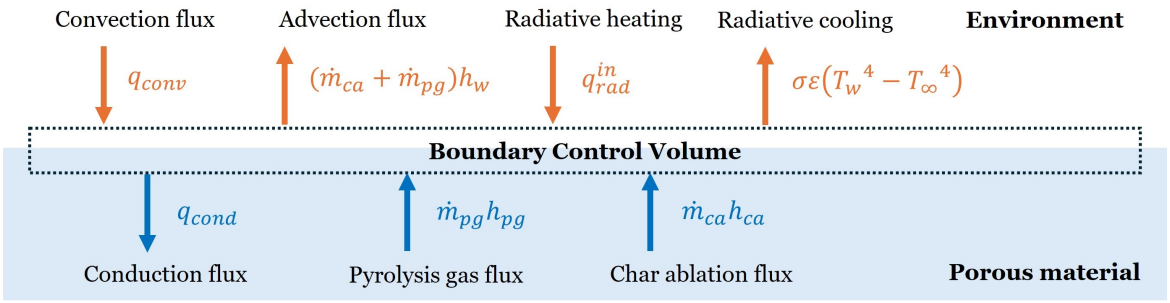


Figure 3.4: Schematic of energy balance at the boundary

vation of energy at the boundary:

$$\begin{aligned} -\left(\underline{\underline{k}} \cdot \frac{\partial T_w}{\partial \mathbf{n}}\right) \cdot \mathbf{n} =& \rho_e u_e C'_H \left(h_e - h_w\right) + \dot{m}_{pg}\left(h_{pg} - h_w\right) + \dot{m}_{ca}\left(h_{ca} - h_w\right) \\ &+ q_{rad}^{in} - \varepsilon_w \sigma \left(T_w^4 - T_\infty^4\right) \end{aligned} \tag{3.16}$$

where ε and σ are surface emissivity and Stefan-Boltzmann constant, respectively. C'_H is corrected version of Stanton number to account for the blockage induced by the pyrolysis/ablation gas flux. The correction form used in PATO with scaling factor (λ) equal to 0.5 [7] is provided:

$$C'_H = C_H \ln\left(1 + 2\lambda B'\right) / \ln\left(2\lambda B'\right) \tag{3.17}$$

$$B' = \left(\dot{m}_{pg} + \dot{m}_{ca}\right) / \left(\rho_e u_e C_M\right) \tag{3.18}$$

where B', C_H, C_M denote dimensionless mass flow rate, Stanton number for heat transfer, and Stanton number for mass transfer, respectively.

The "Bprime" boundary condition involves defining the variables $\rho_e u_e C_H$, h_e, q_{rad}^{in}, and the heat convection coefficient at the boundary, and solving for the wall temperature and recession rate based on the properties of the environment and the ablative material. Utilizing this boundary condition for the study is discussed in Section 4.2.2.

3.3 Applications

PATO has been employed in various applications, including biomass pyrolysis [29], ablative materials [29, 30], carbon fiber oxidation [27], and thermal response in high-speed environments [32]. Among these, biomass pyrolysis and ablative materials offer valuable insights for modeling nanothermite combustion, which will be examined in the following sections.

3.3.1 Biomass Pyrolysis

Biomass pyrolysis is a thermochemical process that involves the decomposition of organic materials at elevated temperatures in an oxygen-deprived environment, resulting in the production of biochar, bio-oil, and syngas. This process plays a pivotal role in the conversion of biomass into valuable products and renewable energy sources [36].

Although biomass pyrolysis and nanothermite combustion involve different materials and produce distinct outputs, both processes are governed by fundamental principles of heat and mass transfer, along with complex chemical reactions. Both cases deal with porous structures and gas production resulting from the decomposition of solid materials during the reaction. Precise temperature regulation and detailed reaction modeling are essential in each instance to optimize outcomes. For nanothermite combustion, several features of PATO in modeling biomass pyrolysis can be effectively applied to enhance process understanding and optimization [29]:

- **Heat Transfer Simulation**: Nanothermite reactions, characterized by rapid temperature escalation and substantial energy release, benefit from PATO's advanced

heat transfer modeling capabilities. These simulations provide precise predictions of temperature profiles and thermal effects, including conduction, convection, and radiation, which are essential for the design of controlled combustion systems.

- **Chemical Reaction Modeling**: Although the chemical species involved differ, PATO's comprehensive kinetic models for biomass pyrolysis can be adapted to simulate the reaction mechanisms in nanothermite materials and the resulting formation of multiphase products. This adaptation aids in optimizing energy release and enhancing control over reaction rates.

- **Mass Transfer Analysis**: Similar to biomass pyrolysis, nanothermite combustion involves gas evolution, particularly during oxidation or reduction reactions. PATO's mass transfer modeling capabilities can predict the diffusion and movement of gases through the porous material matrix, thereby ensuring efficient propagation of the reaction.

3.3.2 Ablative Materials

Ablative materials are designed to protect structures from extremely high temperatures by undergoing controlled degradation, where the material surface erodes and absorbs heat, forming a protective char layer. These materials are essential in aerospace applications, such as thermal protection systems for re-entry vehicles [34].

The simulation of ablative materials shares a common focus with the combustion of nanothermite pellets, as both involve surface mass degradation occurring under extreme conditions. Figure 3.5 illustrates a range of phenomena in ablative materials that PATO is capable of capturing at various levels of detail. The erosion and thermal response of ablative materials under extreme heat fluxes reflect the challenges associated with controlling temperature during the ignition and sustained combustion of the pellet. In the case of nanothermite combustion, PATO's capabilities are particularly relevant for [29, 30]:

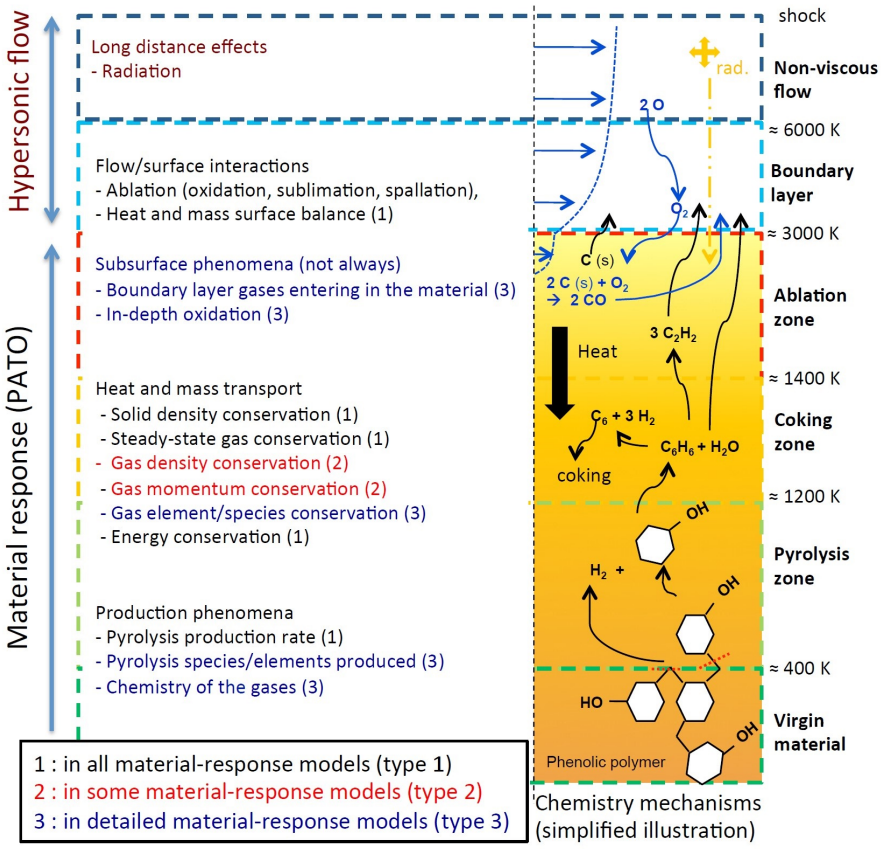


Figure 3.5: Modeling levels of different phenomena in porous carbon/phenolic ablative materials [30]

- **Ablation and Material Degradation**: The surface recession rate and mass degradation in nanothermite combustion can be effectively modeled using the "Bprime" boundary condition, which is employed in the simulation of ablative materials. This allows for accurate predictions of material behavior under high-temperature conditions, aiding in the optimization of nanothermite performance.

- **Thermal Response Modeling**: A thermal model for the surface would capture the energy loss due to ablated condensed phase, in addition to addressing heat transfer mechanisms like conduction, convection, and radiation. This ensures a comprehensive simulation of the thermal behavior during nanothermite combustion, improving predictions of burn rate and energy efficiency.

Although these applications may appear unrelated at first, they share fundamental physical and chemical phenomena similar to those observed in nanothermite combustion. PATO's versatile modeling framework can be effectively utilized to analyze and enhance the combustion characteristics of nanothermites, ultimately contributing to improved control and efficiency in their application. The next chapter provides a detailed explanation of the proposed model and outlines the application of PATO for simulating nanothermite combustion.

Chapter 4

Proposed Model

This chapter introduces the conceptual framework and mathematical formulations developed to accurately capture the key physical and chemical processes involved in nanothermite pellet combustion. Building upon the governing equations discussed earlier, this model extends PATO presented in Chapter 3, incorporating additional assumptions, parameters, and boundary conditions to address the specific challenges of this work. The following sections will provide a detailed explanation of the model's components and the rationale behind their selection, highlighting how PATO has been adapted to suit the unique characteristics of nanothermite combustion.

4.1 Conceptual Framework

As discussed in Section 1.1, nanothermite can be structured in various forms. For example, it may consist of physically mixed nanoscale metal fuel and oxidizer powders uniformly distributed through different mixing techniques or as core-shell structures, where a metal fuel core is encased by an oxidizer shell, with each configuration yielding unique combustion characteristics [56]. In the case of physically mixed nanothermites, the powders may agglomerate into micron-scale structures during the mixing process [33], and the resulting

mixture is then pressed into dense, solid pellets. The term *theoretical maximum density (TMD)* is the highest possible density that a material can achieve when all pores within the structure are eliminated, meaning the material is in its most compact and efficient form. It depends on the intrinsic densities of the metal fuel and oxidizer and their proportions in the mixture. TMD serves as a benchmark in the design and production of nanothermite pellets, with Table 1.1 providing the values for some thermites. The other term *porosity (ϕ)* is commonly used in porous media studies to refer to the volume fraction of pores within a material relative to its total volume:

$$\phi = \frac{V_{pores}}{V_{total}} \tag{4.1}$$

The products of most thermite reactions exist in both gaseous and condensed phases (either liquid or solid), thereby presenting a multiphase problem. To simplify the analysis, following the approach proposed by Epps *et al.* [14], we assume a solid/gas system in which all condensed phase products are treated as a porous-structured solid material and gas products fill the pores.

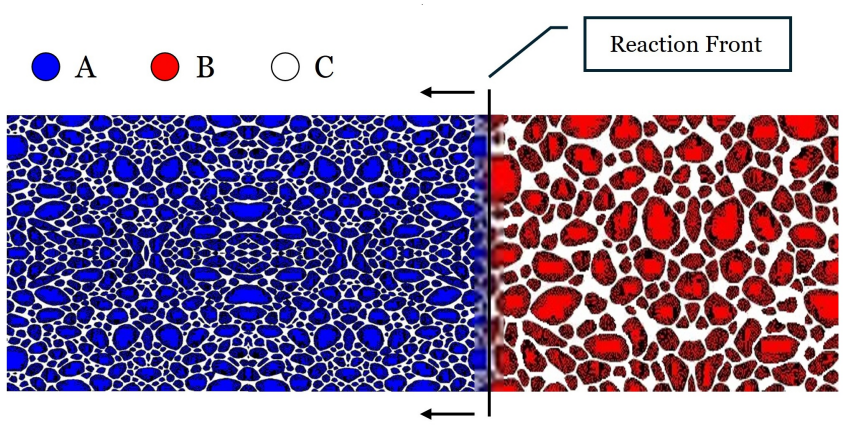


Figure 4.1: Solid/gas framework of thermite combustion model

The thermite combustion process can then be summarized by the following chemical reaction:

$$\mathrm{A_{(s)}} \longrightarrow \mathrm{B_{(s,l)}} + \mathrm{C_{(g)}} \tag{4.2}$$

where A and B represent pre- and post-combustion condensed phases, respectively, and C represents gaseous phase. The indices 's', 'l', and 'g' denote solid, liquid, and gas states of matter, respectively. Figure 4.1 illustrates the schematic of the discussed model framework. Material modeling in PATO addresses the properties of condensed phases before and after combustion, with solid properties during the reaction calculated based on these two states. In order to avoid lengthy descriptions, we refer to A as *virgin* and B as *residue* in this study to align with PATO's framework.

4.2 Simulation Details

As discussed in Chapter 3, PATO was employed to conduct the simulations in this study. The PATO model's flexibility allowed for its adaptation to incorporate the proposed thermite combustion model framework. The conservation of mass, momentum, and energy, as outlined in Section 3.2, served as the governing equations for the model. The specifics of model implementation are elaborated upon in the following subsections.

4.2.1 Model Parameters

The combustion of Al/CuO nanothermite is a highly exothermic reaction characterized by the following chemical equation:

$$2\,\mathrm{Al} + 3\,\mathrm{CuO} \longrightarrow \mathrm{Al_2O_3} + 3\,\mathrm{Cu} \tag{4.3}$$

By using the standard enthalpies of formation for copper oxide (-156.06 kJ/mol) and alumina (-1675.69 kJ/mol), the theoretical enthalpy of combustion for the Al/CuO thermite reaction is calculated to be 4.127 kJ/g. Considering the adiabatic flame temperature of 2843 K [17], along with the approximate melting and vaporization points of alumina (2327 K, 3250 K, respectively) and copper (1358 K, 2835 K, respectively), it can be reasonably inferred that alumina will not reach its boiling point under these conditions. Furthermore,

the analysis focuses on macro-scale flame propagation, which is primarily governed by heat transfer mechanisms such as conduction and convection. The combustion reaction time scale is significantly shorter than that of flame propagation. As a result, this study does not investigate the transient formation of intermediate gas-phase species prior to the completion of the reaction. Consequently, assuming complete combustion of the reactants, it is reasonable to conclude that the gas phase will predominantly consist of metallic copper vapor.

The reaction advancement (χ) is assumed to follow the Arrhenius form, as presented in Equation 3.4, with a single phase decomposition similar to the approach used by Kim [23]. The parameters $\mathcal{A}$, $\mathcal{E}$, m, and n are set to 4.89×10^{-6} 1/s, 48 kJ/mol, 1, 0, respectively. Consequently, the evolution of solid phase in Equation 3.3 and the source term in Equation 3.5 can be determined solely by the pyrolysis term $\epsilon_{s,0}\rho_{s,0}F\partial_t\chi$. Due to the high energy release and the temperature exceeding copper's boiling point, all the copper product will evaporate upon reaction completion at the flame front. Consequently, the solid phase will lose its corresponding mass fraction, resulting in F being 0.6515 (product mass fraction: 34.85% Al_2O_3, 65.15% Cu). It is noteworthy that the convected gas into the unburnt section of the pellet may condense back into the liquid phase. However, the current model treats this material as a gas, incorporating its correct specific heat and accounting for the latent heat of phase change in the calculations.

In the analysis, it is assumed that the virgin consists of a stoichiometric mixture of aluminum and copper oxide (reactant mass fraction: 18.44% Al, 81.56% CuO), with a TMD of 5109 kg/m^3. The residue is identified as alumina, while the gas phase is copper. The specific heat capacities (c_v, c_p) and enthalpies (h) for the virgin, residue, and gas phase over the simulated temperature range (300 $\sim$ 3000 K) have been obtained from National Institute of Standards and Technology (NIST) Chemistry WebBook[1] [6]. Enthalpies of fusion and vaporization are included in the property tables to prevent overestimating flame temperature. Material phase changes are incorporated into the thermodynamic properties,

[1] https://webbook.nist.gov/chemistry

without altering the solid/gas model structure.

The porosities (ϕ) of the virgin and residue depend on the packing density of the pellet. For virgin, porosity is equivalent to the initial volume fraction of the gas phase. For residue, due to the differing densities of copper and alumina and subsequent calculations, it is assumed that approximately 47% of the virgin solid volume will be added to the pore volume in residue. For instance, in a case with packing density of 30% TMD, the porosities of the virgin and residue would be 0.7 and 0.841, respectively.

In this study, the pellet is treated as an isotropic solid. Consequently, the parameters $\underline{\underline{K}}$ and $\underline{\underline{k}}$ are represented as isotropic tensors, with identical values of K and k in all diagonal components. The permeability (K) is typically determined experimentally for porous media. However, due to the scarcity of experimental permeability data for nanothermite pellets, the Kozeny-Carmen equation provides a way to relate the porosity of a packed bed of uniform spheres to the permeability of porous structures [22, 35]:

$$K = \frac{\phi^3 d_c^2}{k_k(1-\phi)^2} \tag{4.4}$$

where k_k and d_c are Kozeny constant and characteristic pore size, respectively. The Kozeny constant is meant to capture details about the flow path, particle shape, and connection. While it is recognized that the formula was not specifically developed for this case, it will still provide a rough order of magnitude estimation for permeability due to the lack of validated data. In this analysis, values of 1 µm and 72 are used as the characteristic pore size and Kozeny constant, respectively, with the Klinkenberg correction being neglected ($\beta = 0$). Subsequently, the permeabilities of virgin and residue can be calculated based on their respective porosities.

Due to the lack of precise data for the viscosity of copper in the gaseous phase, a value of 10^{-5} Pa.s is assumed, corresponding to the typical order of magnitude for gases such as oxygen and nitrogen at approximately 3000 K. Simulations indicate that uncertainty in the ratio of permeability to viscosity (K/μ), used to calculate Darcian flow velocity, has minimal impact on flame propagation speed, provided that values are within the correct order of magnitude.

Modeling thermal conductivity (k) in thermite pellets presents significant challenges due to the intricate interplay of reactive materials and their microstructure. Nonetheless, precise characterization of thermal conductivity is essential for accurately predicting flame speed and the dynamics of the combustion. In real scenarios, the liquid portion of the condensed phase typically has a lower thermal conductivity compared to the solid portion; however, it contributes to heat transfer to adjacent cells through liquid convection [13], a factor not considered in this study. Therefore, a reasonable approach would be to use an average effective value of conductivity that compensates for the limitations of solid/gas framework in the model. In the baseline case, the value of 65 W/m.K is selected for thermal conductivity as used by Epps *et al.* [14].

In the conservation of energy Equation 3.12, the diffusion term is neglected, and heat production from the reaction 4.3 is included as a source term ($\dot{S}$). For each computational cell, the reaction advancement (χ) is the key parameter used to calculate the heat production source term and solid phase properties. Two sample formulas for deriving solid phase properties from virgin and residue phases are provided, with the full set available in PATO's user guide under the material properties model for porous type.

$$c_{p,s} = c_{p,v} + \chi \left(c_{p,r} - c_{p,v} \right) \frac{\rho_v}{\max \left(\rho_s, \rho_r \right)} \tag{4.5}$$

$$K_s = K_v + \chi \left(K_r - K_v \right) \tag{4.6}$$

where the indices 's', 'v', and 'r' represent the corresponding variables for solid, virgin, and residue, respectively.

In this study, the properties specific to an Al/CuO nanothermite pellet are utilized, although the model can be generalized to apply to any gas generating thermite. The simulated scenarios include nanothermites with packing densities ranging from 10% to 80% TMD, covering the range that is typically experimentally achievable and of interest [1, 53].

4.2.2 Geometry, Boundary, and Initial Conditions

Since the pellets used in the experimental studies about thermite combustion are mostly cylindrical [40], a two-dimensional axisymmetric approach was chosen for the model. The simulation domain has a radius of 1 mm and a height of 3 mm (Figure 4.2.a). This configuration ensures a stable reaction propagation velocity within the pellet in all simulated scenarios while maintaining a manageable computational load. OpenFOAM recommends using a 5-degree wedge to simulate a cylindrical domain with no variation in the angular direction (Figure 4.2.b), significantly reducing computational cost compared to modeling the full 3D cylinder [18]. Due to symmetry, the results from the wedge domain can be extended to the full cylinder, with the two wedge boundaries serving as symmetry planes (adiabatic and impermeable).

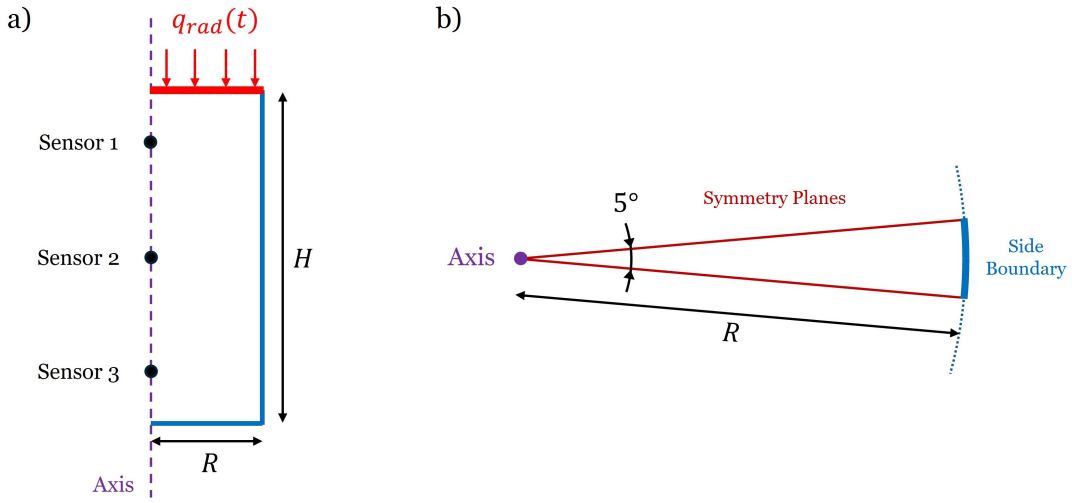


Figure 4.2: Schematic of 2D axisymmetric pellet geometry: a) front view, b) top view

In this study, the term *flame* refers to the propagation of the reaction front during combustion. To determine the average flame speed, two computational probes are positioned 0.5 mm from the top and bottom boundaries in order to minimize the influence of boundary conditions. Additionally, a probe is placed at the center of the pellet to measure

and compare the maximum flame front pressure across all scenarios.

Initially, the pellet is at a temperature of 300 K, and the internal pressure is at atmospheric level. The top, side, and bottom boundaries are exposed to atmospheric pressure, natural convective heat transfer with a coefficient of 5 W/m^2K, and radiation to an environment at 300 K. The top boundary follows a two-stage boundary condition: A constant heat flux of 400 MW/m^2 [40] is applied to simulate laser ignition of the pellet, which is discontinued upon the onset of flame propagation. The turn-off point for the laser, representing the ignition delay, is determined through a trial-and-error method with a precision of 1 µs, ensuring sufficient time for the flame to become self-sustaining (Table 4.1). The following energy equation is applied to the boundaries:

$$-\left(\underline{\underline{k}} \cdot \frac{\partial T_w}{\partial \mathbf{n}}\right) \cdot \mathbf{n} = h_{conv}\left(T_e - T_w\right) + q_{rad}^{in} - \varepsilon_w \sigma \left(T_w^4 - T_\infty^4\right) \tag{4.7}$$

where q_{rad}^{in} has a non-zero value for the top boundary before the laser turn-off point. To prevent computational complications due to a sudden change in the boundary condition, the value is gradually reduced to zero using a linear ramp over 1 µs.

To account for residue ablation as an alternative scenario, the Bprime boundary condition, as described in Section 3.2.2, is applied to the top boundary after the laser is turned off. Since the boundary recession, as formulated by Equation 3.15, is defined in a single direction and mesh movement and resizing within the domain depend on these boundary changes, the simulation achieves convergence within a 1D axial framework, which effectively captures flame propagation across the domain. Both 2D axisymmetric and planar simulations, incorporating residue ablation based on this model, were also tested. However, due to the curved shape of the flame front near the side boundaries, a different recession rate must be applied to the top boundary cells, which disrupts the integrity of the computational grid and leads to rapid divergence once flame propagation begins. In addition to these scenarios, a 1D simulation without residue ablation is performed to compare and evaluate the effects of ablation on flame propagation.

Experimental tests indicate that, after complete pellet combustion in an open tube, only a negligible amount of matter remains at the reaction site [40]. This is attributed

to the dispersal of combustion gases, driven by a high-pressure gradient that carries away residues from the weakened pellet structure. In the modeled scenario with ablation, hot combustion residues exit the computational domain through the top boundary, causing the pellet to shrink as the flame propagates through the domain. Consequently, the exit mass flux variable ($\rho_e u_e C_H$) must be adjusted to ensure that the flame propagation speed aligns with the recession rate of the top boundary. As ablation intensity increases from zero, the recession rate rises while the flame propagation speed decreases, reaching a point where the movement of the top boundary matches the flame front. Table 4.1 presents the exit mass flux values, determined through trial and error with an accuracy of 200 kg/m^{2}s, that achieves this alignment. This level of accuracy represents the threshold at which changes in the movements of the top boundary and flame front become visually observable.

Table 4.1: Imposed values of ignition delay and exit mass flux for top boundary conditions

% TMD	10	20	30	40	50	60	70	80
$t_{ign} \times 10^{-4}$ [s]	0.60	0.92	1.16	1.38	1.59	1.77	1.96	2.12
$\rho_e u_e C_H \times 10^4$ [kg/m^{2}s]	1.02	1.34	1.60	1.84	2.06	2.26	2.44	2.60

Different types of nanothermites may experience varying intensities of ablation during combustion. To examine the effect of ablation intensity on flame propagation speed and peak pressure, additional scenarios with 75%, 50%, and 25% of the exit mass flux values listed in Table 4.1 were also analyzed.

4.2.3 Grid, Solvers, and Discretization Schemes

The computational grid for each scenario is specifically adjusted to optimize computational load and ensure data convergence. Near the flame, the grid size must be refined to capture the highest gradients in the domain. For 2D and 1D scenarios without ablation, a uniform axial discretization is used due to the static mesh and the flame traveling across the entire

domain. In contrast, for the 1D scenario with ablation, the domain shrinks as the flame propagates and the boundary moves with the flame, allowing a finer grid near the top boundary where both ablation and flame are present. Additionally, the radial discretization of the 2D domain is finer near the side boundary, as it encounters higher gradients than the centerline. Figure 4.3 presents coarse examples of the mesh structure for each scenario, illustrating the meshing approach used.



Figure 4.3: Coarse examples of computational grid for each scenario

Cases with varying packing densities experience different pressure gradients and gas convection velocities within the pores. Therefore, using a finer mesh for cases with higher packing densities is preferable to applying a uniform mesh across all cases. In 2D-axisymmetric scenario, the grid is adjusted from 85×300 for the 10% TMD case to 200×700 for the 80% TMD case in the radial and axial directions, respectively, with smaller cells concentrated near the side boundary. In 1D scenarios, the number of cells increases from 1000 for the 10% TMD case to 4000 for the 80% TMD case. This setup balances computational efficiency with the necessary resolution. A mesh sensitivity study, discussed in Section 4.3, is conducted to confirm that the results are independent of the mesh size beyond a certain

threshold.

The time step (Δt) is updated in each iteration based on the Courant number (Co), defined as follows:

$$Co = \frac{|\mathbf{v_g}|\,\Delta t}{\Delta \mathbf{x}} \tag{4.8}$$

The use of a variable time step eliminates the need for small time steps before flame propagation begins. Given the variation in computational cell size and gas convection velocity across the domain, the time step is adjusted to maintain a Courant number below the maximum threshold of 0.1 in all cells. This criterion ensures convergence across all simulation cases, with time steps ranging from 10^{-9} to 10^{-11} seconds during flame propagation.

Following similar published cases involving ablative materials, the pressure and temperature solvers employed in the simulations are the stabilized preconditioned bi-conjugate gradient (PBiCGStab) method [49] with a simplified diagonal-based incomplete LU (DILU) preconditioner, well-suited for handling asymmetric matrices. The time derivative discretization uses an Eulerian approach, while gradient, divergence, and Laplacian terms are discretized using linear Gaussian methods.

4.3 Validation

Standardized benchmark cases in the open literature for validating heat and mass transport with chemical reactions in porous media are highly limited. In the field of consolidated nanothermite combustion, benchmarking is unavailable, and few numerical models have been developed to simulate specific cases, primarily focusing on combustion effects on the environment and thrust generation. The numerical solvers of PATO have been tested in various applications, including biomass pyrolysis, ablative materials, carbon fiber oxidation, and simple heat and mass transport phenomena. However, the application of PATO to solid fuel combustion is novel in this study.

A basic numerical model with a fundamental structure similar to the thermite combustion model used in this study was simulated by Epps *et al.* [14] using in-house code.

Figure 4.4 presents the reproduced result of the baseline case with a characteristic pore size of 1 µm from their study, using PATO solvers. The average flame speeds from PATO results at different packing densities are in good agreement with those from the mentioned study.

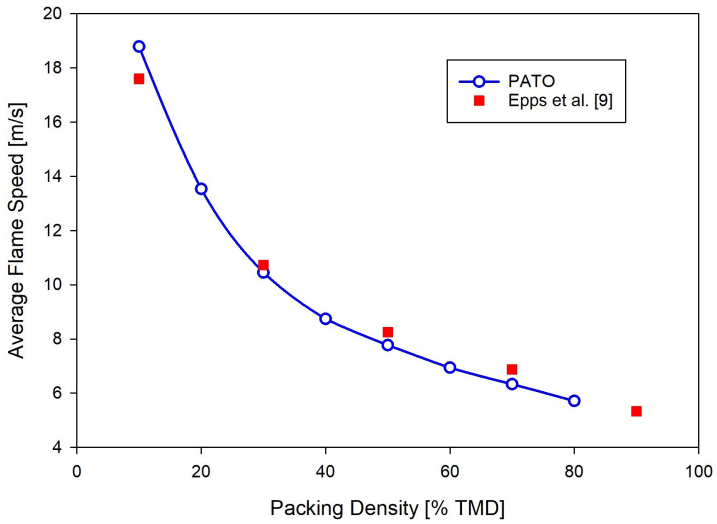


Figure 4.4: Reproduction of Epps *et al.* [14] results of average flame speed in PATO

The current model in this study includes several more complex improvements, some of which are listed as follows:

- Residue removal from the domain via ablation
- Different structures for pre- and post-combustion condensed phases
- Spatially varying properties of condensed phases, such as porosity, permeability, etc.
- Adjustment of gas production rate with precise tabular properties
- Consideration of phase change enthalpies in both condensed and gaseous phase property tables

- Inclusion of radiation heat transfer in boundary conditions
- Well-established numerical solvers tailored for porous media applications.

These improvements enhance the accuracy and realism of the model, allowing for a more comprehensive simulation of combustion dynamics in porous media. By incorporating these factors, the model can better represent complex physical phenomena such as ablation, phase changes, and heat transfer, leading to more reliable predictions of flame behavior and pressure profiles under various conditions.

In numerical modeling, obtaining accurate and reliable results often depends on the resolution of the computational grid. To evaluate the impact of cell count on key output parameters, a mesh sensitivity study, shown in Figure 4.5, is conducted on a 10% TMD pellet. Given the non-linear nature of Equation 3.5 with respect to the pressure and the presence of substantial pressure gradients within the domain, the flame peak pressure at the pellet center is selected as the output parameter to assess mesh independence.

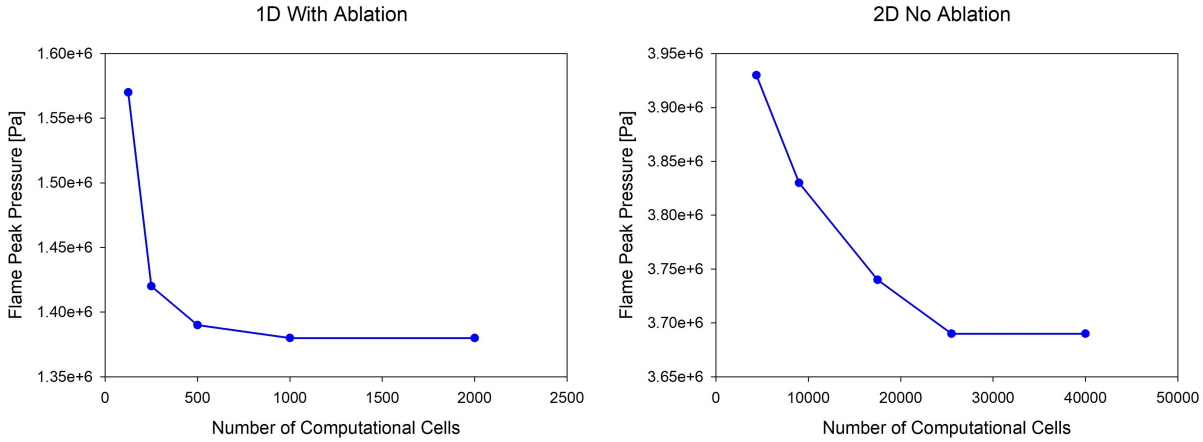


Figure 4.5: Mesh sensitivity study on flame peak pressure for 10% TMD pellet

The figure presents two scenarios: a 1D model with ablation and a 2D-axisymmetric model without ablation. In the 1D scenario, flame peak pressure stabilizes at approximately 1000 cells, indicating that further refinement has minimal influence on pressure

values. In the 2D scenario, the flame peak pressure initially decreases with increasing cell numbers but reaches stability around 25,500 cells. This analysis suggests that, beyond a certain mesh resolution, further refinement does not significantly alter results, underscoring the importance of an appropriate mesh density to ensure accuracy while minimizing computational load.

For cases with higher packing densities, determining the appropriate mesh size becomes more straightforward. A set of grids with 1000, 1500, 2000, 3000, and 4000 cells for the 1D scenario, and grids with 85×300, 100×400, 140×500, 170×600 and 200×700 cells for the 2D scenario, are used in the simulations. For each packing density case from 20% to 80% TMD, simulations are conducted with two mesh configurations: the grid used in the previous case and a finer option from the set. Based on the results, the optimal mesh size is selected for each specific packing density, with criteria including simulation convergence, smooth flame propagation, and stable flame peak pressure.

Chapter 5

Results and Discussion

This chapter presents and analyzes the results of numerical modeling of Al/CuO nanothermite pellet combustion using PATO. The study examines key parameters influencing flame propagation speed, pressure dynamics, and thermal profiles within the pellet, with a focus on understanding the effects of pellet packing density and residue ablation. The results provide insights into optimizing computational setups for nanothermite combustion simulations and contribute to the development of more precise predictive models for solid fuels with high energy density. Additionally, the sensitivity of key parameters, such as Stanton number, thermal conductivity, and permeability/viscosity ratio, on the simulation outcomes is explored, shedding light on their role in governing flame behavior and combustion efficiency.

5.1 Baseline Simulation Scenarios

The simulations begin with ambient temperature and pressure conditions throughout the domain, with a laser energy flux applied to the top boundary. As the chemical reaction follows the Arrhenius law, a time delay is required before the temperature in the top layer of the nanothermite pellet rises sufficiently to initiate substantial gas production and heat

release. This reaction enables adjacent cells to reach similar conditions without further laser induction and a self-sustained combustion takes place.

Figure 5.1 illustrates an approximately linear relationship between packing density and ignition delay. Although the solid mass in the pellet increases linearly with packing density, the ignition delay does not follow an exact linear trend. This slight deviation arises because, at higher packing densities, the increased gas production and reduced void space limit the accumulation of produced gases prior to ignition. As a result, a greater pressure gradient forms within the gas phase, causing a portion of the gas to exit the top layer before it reaches full heating. This process allows the laser to elevate the temperature of the top layer more rapidly, as some mass is lost, resulting in a slightly lower ignition delay than expected from a purely linear trend. Consequently, the slope between data points in Figure 5.1 decreases slightly from 10% to 80% TMD.

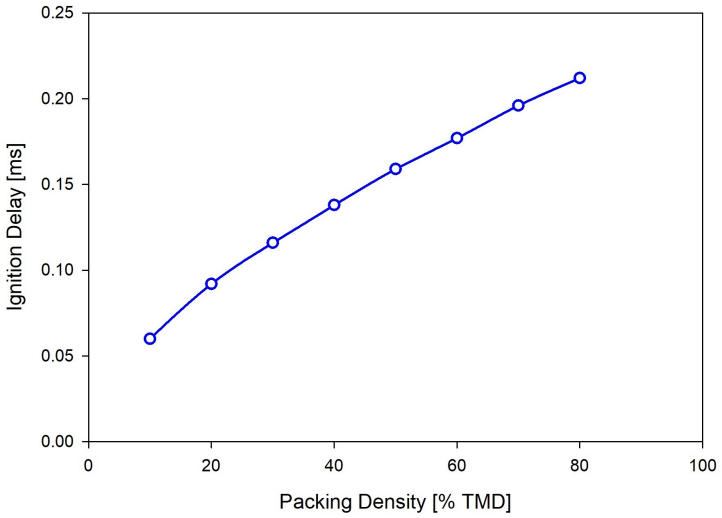


Figure 5.1: Effect of pellet packing density on ignition delay

The ignition delays presented in this model are in complete agreement with the numerical study conducted by Epps *et al.* [14]. Although the results follow the same semi-linear trend of ignition delay versus packing density as observed in experimental studies [40],

they deviate quantitatively by approximately an order of magnitude, possibly due to the omission of laser ablation effects in this model. Laser ablation likely removes surface mass before it can effectively conduct heat into the inner layers of the pellet, thereby delaying the ignition of sustained combustion.

After ignition occurs and the laser heating flux ceases, the reaction front progresses toward the bottom of the pellet, driven by energy transport through conduction and gas convection within the pores. Numerical probes are used to capture the temperature and pressure evolution at specific points within the domain. As illustrated in Figure 4.2.a, probes 1 and 3 are positioned 0.5 mm from the top and bottom boundaries, respectively, with probe 2 placed at the center of the pellet. Figure 5.2 presents example output data from probes 1 and 3 in the 2D scenario without ablation for a pellet with 10% TMD.

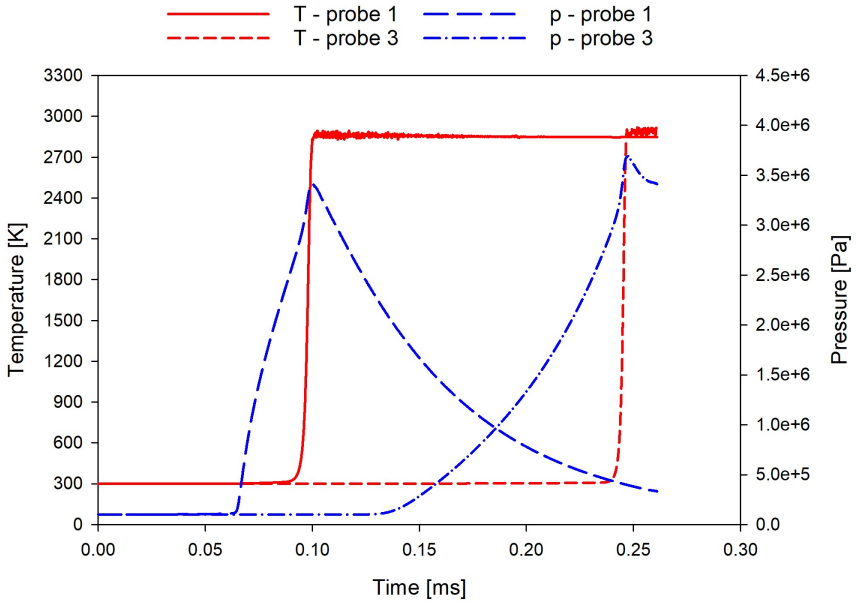


Figure 5.2: Temperature and pressure evolution at probes 1 and 3 for 10% TMD pellet (2D scenario without ablation)

The average flame propagation speed within the pellet can be calculated based on the time difference between the peak pressures or temperatures recorded by the two probes

positioned 2 mm apart. Figure 5.2 shows that the probes detect the onset of pressure rise well before the reaction peak, indicated by a steep temperature increase resulting from substantial heat release. This suggests that hot gases generated at the upstream flame front convect through the porous medium, preheating the unburned region and thereby promoting combustion. Additionally, simulations reveal that pressure peaks occur a few time steps before the maximum temperature is reached, marking the conclusion of reaction. The gases generated during combustion increase pressure within the pores ahead of the flame front, driving Darcian flow through the pores even before the reaction is complete.

The flame peak temperature across all cases is slightly higher than the reported adiabatic flame temperature of Al/CuO nanothermite (2843 K [17]), but consistent with the findings of Wang *et al.* [50] in their experimental study. This supports the assumption of a gaseous copper phase in the model, with a vaporization point of 2835 K. The increase in flame peak pressure along the pellet axis, due to the accumulation of convected gases from the burned region, justifies the positioning of probe 2 at the center of the pellet. This placement enables consistent comparison of flame peak pressure across all cases and scenarios while minimizing boundary effects.

Another important observation is the time scale of thermite reaction in comparison to flame propagation. As shown in Figure 5.2, the reaction progression occurs as a sharp temperature increase, with the majority of the reaction, excluding the initial 10%, taking place on the microsecond time scale. However, the time scale of flame propagation, driven by conduction and gas convection, is around 0.1 milliseconds. This observation supports the assumption of neglecting the intermediate gas species of combustion and focusing on the products of the completed reaction.

To examine the smooth propagation of the flame within the domain, the local flame speed is calculated for various cases. Figure 5.3 illustrates the local flame speed at intervals of 0.1 mm along the pellet length for 10%, 30%, 50%, and 70% TMD cases in both the 1D scenario with ablation and the 2D scenario without ablation. By selecting an appropriate mesh size for each case, the model successfully achieves stable flame propagation with

minimal fluctuations in speed throughout the pellet, except near the top and bottom boundaries. The choice of probe positions 1 and 3 to measure average flame speed is clearly justified by the results presented in Figure 5.3.

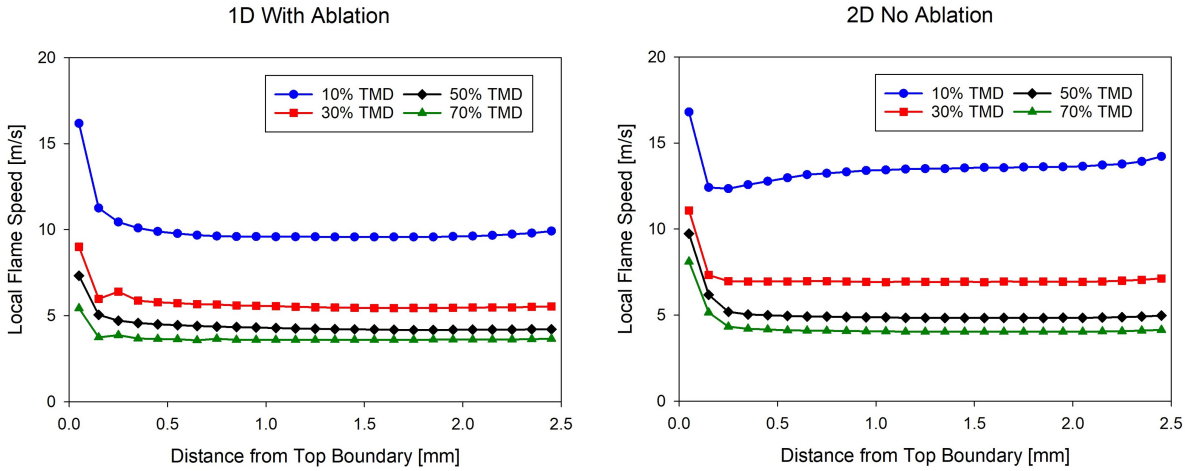


Figure 5.3: Local flame speed with respect to distance from top boundary

The elevated burn rate observed near the top boundary may be attributed to the initial atmospheric pressure within the pores, which facilitates the inward transport of convective gas from the burned region with minimal resistance. Given that conductive heat transfer between adjacent cells remains consistent throughout the domain, this variation is due to the energy transported by gas convection. As the flame advances from the boundary, the increasing internal pressure within the pellet begins to resist the inward flow of gas, eventually reaching a balance between the pressure gradient and convective gas flow, which results in a stable flame propagation speed. A similar behavior is observed near the bottom boundary, where the flame slightly accelerates as it approaches the end of the pellet. The imposed atmospheric pressure as a boundary condition at the bottom provides an easier escape route for the gases generated during combustion.

Figure 5.4 presents a comparison of the average flame speed and flame peak pressure at the center of the pellet across all scenarios: 2D/1D without ablation and 1D with ablation, for cases ranging from 10% to 80% TMD. An increase in pellet packing density

leads to greater gas production within a reduced void space, resulting in a higher flame peak pressure. This also creates a steeper pressure gradient between the flame front and the surrounding environment, increasing the convection flow of hot gases. Consequently, a larger portion of the generated gas exits the domain rather than traveling inward to preheat the unburned region, thereby decreasing the flame propagation speed.

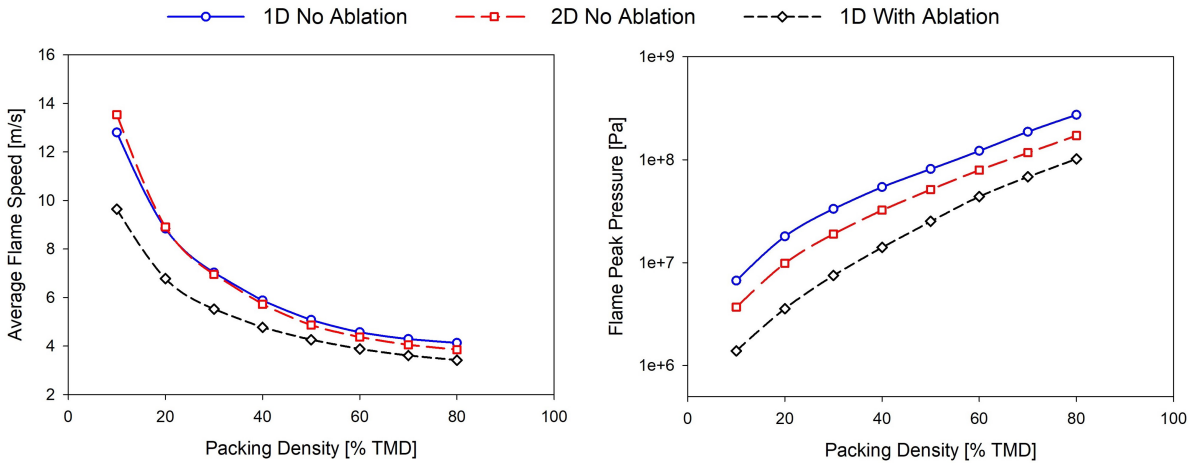


Figure 5.4: Effect of pellet packing density on average flame speed and peak pressure

The ablation effect removes combustion residue from the domain, contributing to energy loss in the pellet and keeping the boundary close to the flame front. This removal facilitates the exit of combustion gases, reducing gas accumulation and lowering both flame peak pressure and propagation speed. In 1D and 2D scenarios without ablation, the side boundary in the 2D-axisymmetric domain allows for radial gas convection and provides an additional exit route, resulting in less gas accumulation and a lower flame peak pressure compared to the 1D scenario. However, the effect on flame propagation speed is more complex. In 2D simulations, the lower peak flame pressure facilitates flame propagation by reducing resistance to the inward flow of the gas phase compared to the 1D scenario. On the other hand, the additional exit route for the gas phase counteracts flame propagation by removing part of the energy required to preheat the unburned region. The result of these opposing factors, shown in Figure 5.4, indicates that the flame propagation speed

in 2D simulations varies from being slightly higher than the 1D results at 10% TMD to slightly lower at 80% TMD.

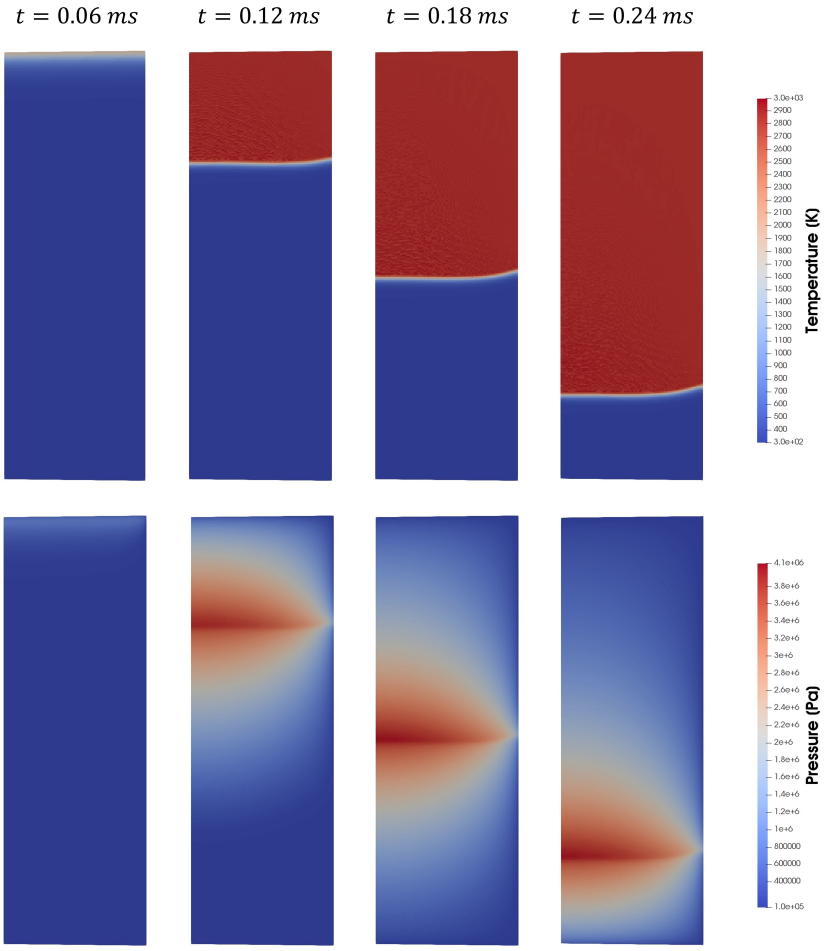


Figure 5.5: Evolution of temperature and pressure contours for 10% TMD pellet (2D scenario without ablation)

Figures 5.5 and 5.6 present the evolution of temperature and pressure contours for 10% TMD case in the 2D scenario without ablation and the 1D scenario with ablation, serving as examples to observe the details of the flame front. In the 2D scenario, as shown in Figure 5.5, the flame speed at the pellet centerline is higher than at the side boundary

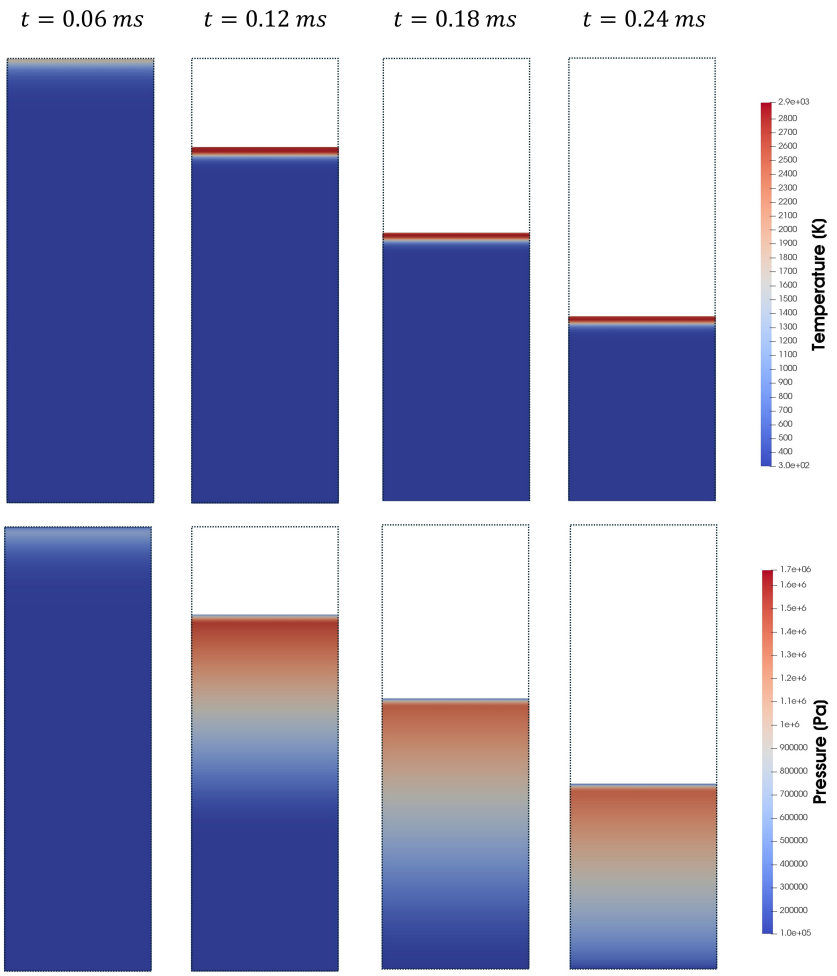


Figure 5.6: Evolution of temperature and pressure contours for 10% TMD pellet (1D scenario with ablation)

due to heat loss and the higher pressure gradient near the boundary. This results in a curvature of the flame front, which originates at the side boundary and intensifies toward the center as the flame propagates. This is the primary reason why the current ablation model cannot be applied to the 2D scenario, as the grid disintegrates due to differing recession rates for the top boundary cells. The curvature becomes more pronounced as the packing density increases. Additionally, the pressure contours around the flame front are asymmetrical, creating a higher pressure gradient in front of the flame to compensate for the lower permeability of the unburned region compared to the combustion residue.

In the 1D scenario, as shown in Figure 5.6, the computational domain reduces in size as the flame progresses. The ablation intensity is set to maintain the top boundary's movement in sync with the flame front once the flame speed stabilizes. Consequently, at the beginning of the pellet, where the flame speed is higher than the stable value, the constant imposed exit mass flux ($\rho_e u_e C_H$) is insufficient to keep the boundary recession aligned with the flame front. Unlike in non-ablation scenarios, the flame peak pressure along the pellet axis decreases due to the discharge of residual mass accumulated during the pellet's initial unstable phase.

One of the key findings of this thesis is that, while the inclusion of ablation effects in the model extends beyond the work of Epps *et al.* [14], the model's predictions for flame speed and ignition delay align with the trends observed in experimental results [40] but fail to quantitatively match the data. Specifically, the numerical results indicate that the flame speed in loose pellets is approximately half of what is observed in experiments. This difference decreases in dense pellets, where heat conduction plays a more significant role compared to convection. These limitations underscore the need for further refinement of the model to incorporate more detailed representations of environment-material interactions and the energetic properties of nanothermites, which could improve its predictive accuracy and better describe experimental observations.

5.2 Parameter Sensitivity

This section explores the sensitivity of key parameters, including the Stanton number, thermal conductivity, and the permeability/viscosity ratio, and their impact on flame propagation behavior. Understanding how these parameters influence combustion processes is crucial for optimizing thermite reaction performance.

The Stanton number represents the intensity of ablation at the top boundary. Figure 5.7 shows a snapshot of temperature contours at a specific time for the 10% TMD case with different ablation intensities, illustrating the impact of ablation intensity on domain recession and flame propagation speed. As ablation intensity increases, the intermediate zone of combustion residue shrinks, making it easier for the produced gas to escape the domain, which leads to a lower flame propagation speed and peak pressure. It also demonstrates the process of determining the appropriate exit mass flux ($\rho_e u_e C_H$) to synchronize the recession rate with the flame front speed. Starting with zero ablation, the intensity is gradually increased until the minimum ablation intensity that satisfies the synchronization condition is identified and applied to the model (Table 4.1). Further increases in this value result in a decrease in flame propagation speed until the energy loss becomes sufficient to extinguish the self-sustaining flame. Additionally, three more ablation intensities, corresponding to 75%, 50%, and 25% of the applied value, are simulated to facilitate comparison with the full-ablation case.

The results for average flame speed and peak pressure in the 1D scenario with different ablation intensities are summarized in Figure 5.8. An important observation in the figure is the gap between the results for 100% ablation intensity and those for lower intensities. The presence of an intermediate zone of combustion residue between the flame front and the environment hinders the escape of produced gases from the domain, resulting in higher flame speed and peak pressure. The impact of this intermediate zone is significant, exceeding the effect of its thickness and explaining the observed gap in results.

As discussed in Section 4.2, the average effective thermal conductivity of nanothermite

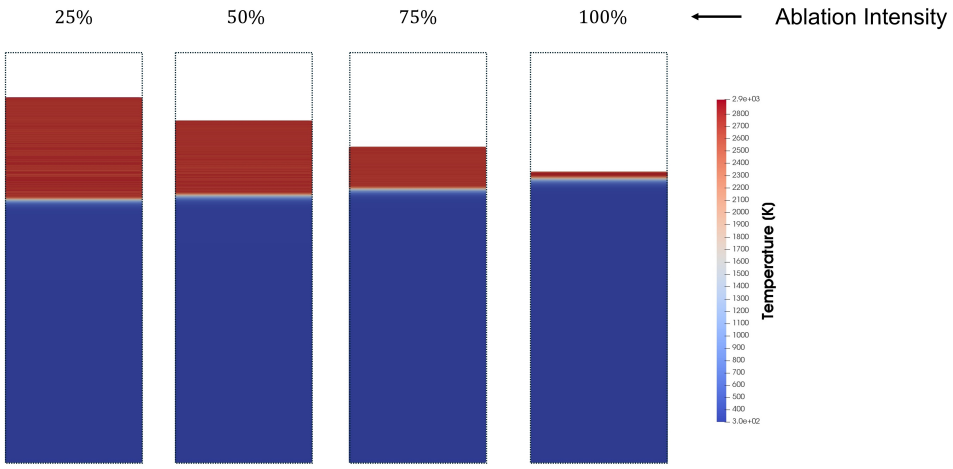


Figure 5.7: Temperature contours at $t = 0.15$ ms for 10% TMD pellet with varying ablation intensity

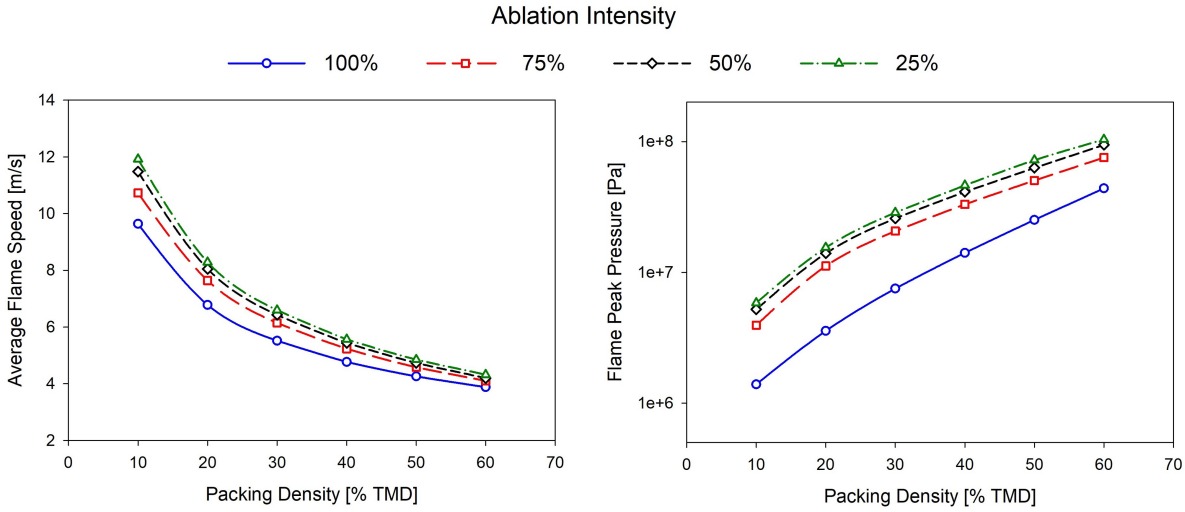


Figure 5.8: Effect of ablation intensity on average flame speed and peak pressure

plays a critical role in governing heat transfer processes and is therefore subjected to a parameter sensitivity analysis in this study. In addition to the baseline value of 65 W/m.K, simulations are also conducted using thermal conductivity values of 40 and 100 W/m.K across various packing densities. The upper bound value corresponds to the maximum thermal conductivity of the pure solid phase without pores [51], while the lower bound is chosen to maintain an approximate ratio relative to the baseline value. Varying the thermal conductivity influences the ignition time and the required Stanton number to maintain the recession rate at the same rate as the flame propagation. Table 5.1 presents the updated values for ignition delay and exit mass flux.

Table 5.1: Updated values of ignition delay and exit mass flux for sensitivity analysis of thermal conductivity

% TMD	10	30	50	70	Thermal Conductivity [W/m.K]
$t_{ign} \times 10^{-4}$ [s]	0.80	1.52	2.08	2.56	100
	0.46	0.87	1.18	1.45	40
$\rho_e u_e C_H \times 10^4$ [kg/m^{2}s]	1.30	2.02	2.54	2.90	100
	0.76	1.24	1.56	1.86	40

Figure 5.9 illustrates the average flame speed for three different thermal conductivity values across various packing densities. An increase in thermal conductivity leads to a longer ignition delay, as the surface material loses more energy to the lower layers through conduction, requiring additional time to reach the necessary temperature to sustain the flame. During flame propagation, increased conduction serves as an effective heat transfer mechanism that accelerates the flame speed. Consequently, the exit mass flux at the boundary rises to match the higher flame speed.

The average flame speed increases by approximately 27% when the thermal conductivity rises from 40 to 65 W/m.K (a 62.5% increase), and by 24% when it increases from 65 to 100 W/m.K (a 53.8% increase). This underscores that conduction is a key mechanism of

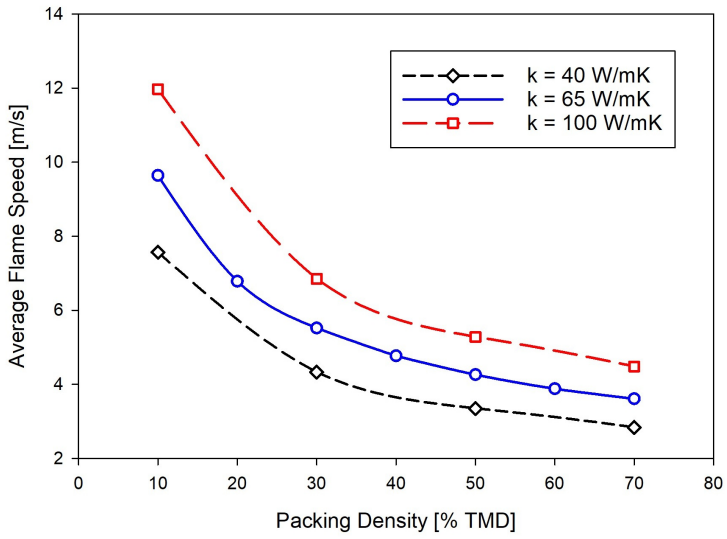


Figure 5.9: Effect of thermal conductivity on average flame speed

heat transfer in flame propagation, though it is not the sole factor influencing flame speed in a strictly linear proportional manner. The simulation results indicate that changes in thermal conductivity impact cases with different packing densities in a comparable way, without revealing a specific or distinct pattern.

To investigate the influence of permeability and viscosity parameters under the uncertainty discussed in Section 4.2, simulations were conducted with the K/μ ratio set to values four times larger and smaller than the baseline case. This proportion is applied to the properties of both the virgin and residue phases, with the boundary conditions remaining unchanged. Table 5.2 summarizes the results of average flame speed for different K/μ ratios, clearly showing that the influence is insignificant. While slightly higher flame speeds were expected with larger permeabilities in all cases, the simulation results do not fully align with these expectations. This discrepancy appears to stem from the accuracy of ignition delay and exit mass flux, which have a more substantial impact on flame speed. Overall, the changes are too minor to form a reliable theory.

On the other hand, the K/μ ratio significantly affects the flame peak pressure, as shown

Table 5.2: Results of average flame speed for different K/μ ratios

% TMD	10	30	50	70	Permeability/Viscosity
Flame Speed [m/s]	9.62	5.56	4.27	3.63	4 K/μ
	9.64	5.52	4.25	3.61	1 K/μ
	9.59	5.54	4.23	3.60	0.25 K/μ

in Figure 5.10. Higher permeability facilitates easier convection of gas through the pores, reduces gas accumulation, and lowers peak flame pressure. In other words, the pressure distribution adjusts to maintain almost the same flame speed in the new configuration. Therefore, the sensitivity study of the K/μ ratio suggests that, for determining the average flame speed, an accurate value of this parameter is not necessary, as long as it is within the correct order of magnitude. It also indicates that permeability can be adjusted in numerical simulations to match the flame peak pressure observed in experimental studies. However, it would be challenging to place a pressure sensor inside a thermite pellet to capture the pressure accurately.

To summarize, the simulation results offer a comprehensive analysis of the complex interplay between packing density, ablation intensity, and combustion dynamics within Al/CuO nanothermite pellets. By systematically exploring parameters such as ignition delay, flame propagation speed, and pressure evolution, this study highlights the critical role of pellet structure and boundary conditions in governing the combustion process. Additionally, the parameter sensitivity study emphasizes the importance of thermal conductivity, Stanton number, and the permeability/viscosity ratio in influencing flame behavior. Overall, this study underscores the importance of tailoring both the physical characteristics and boundary conditions to optimize energy release and combustion stability in nanothermite pellets.

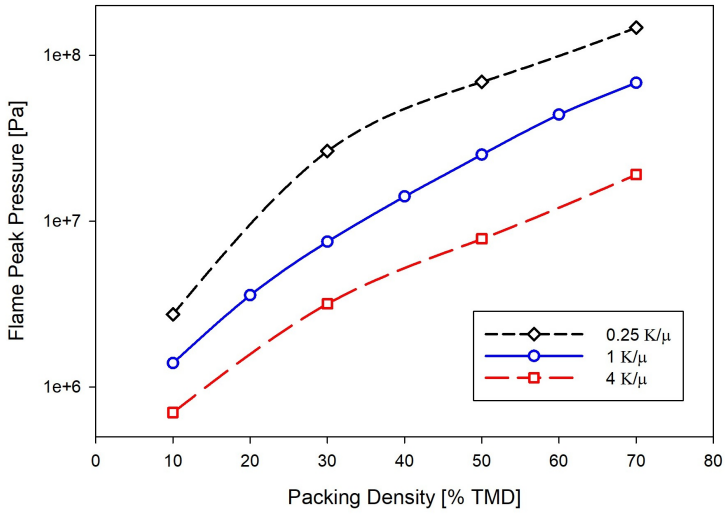


Figure 5.10: Effect of permeability/viscosity ratio on flame peak pressure

Chapter 6

Conclusion

This thesis has presented a detailed investigation into the combustion dynamics of Al/CuO nanothermite pellets, with a specific focus on the role of ablation in influencing performance characteristics. The numerical model developed using PATO provides a novel method for simulating the complex interactions among heat transfer, chemical reactions, and material loss.

Key insights from this research highlight the significant role of ablation in influencing flame propagation, reducing flame speed by approximately 20-25% and altering the flame peak pressure by an order of magnitude. Thermal conductivity was found to affect ignition delay and flame speed, with higher values accelerating flame propagation due to enhanced heat transfer. The permeability/viscosity ratio had a minimal effect on average flame speed but notably impacted the flame peak pressure, indicating that adjusting this ratio could better align simulation results with experimental data. These results emphasize the importance of optimizing packing densities and ablation-related parameters to enhance the performance of nanothermites, particularly in applications such as micro-propulsion and energetics. By simulating various scenarios, the study improves understanding of how material properties and structural configurations influence the stability and efficiency of combustion processes.

An important limitation of the model developed in this thesis is its inability to quantitatively reproduce experimental data for flame speed and ignition delay, despite successfully capturing the observed trends. These quantitative deviations highlight the simplifications and assumptions inherent in the model, particularly in representing ablation effects and the complex interactions between material properties and environmental factors. Addressing these limitations through the incorporation of more detailed physics and improved parametrization could enhance the model's predictive accuracy and enable a more precise replication of experimental results.

This work also contributes to advancing computational methodologies for modeling reactive materials. The integration of ablation-specific boundary conditions within a multiphase framework represents a step forward, bridging existing knowledge gaps and providing tools to predict and control the behavior of nanothermite systems more accurately. However, several challenges and opportunities remain. Experimental validation of the model would strengthen its applicability and provide further confidence in its predictions. Additionally, extending the study to other nanothermite compositions and geometric configurations could broaden its relevance and offer deeper insights into the diverse behaviors of energetic materials. Potential future work includes the following:

- Enhancing the material structure from solid/gas to solid/liquid/gas to account for the liquid condensed phase and its convective effects through porous media
- Incorporating the environmental response of combustion in confined spaces, such as open tubes, to evaluate the thrust generated by combustion.
- Refining the ablation model formulation to enable its application in 2D and 3D simulations.

In conclusion, this thesis not only deepens the theoretical understanding of nanothermite combustion but also lays a foundation for future developments in the design and application of these materials. By addressing both the fundamental dynamics and practi-

cal considerations, it paves the way for safer, more efficient, and more controllable uses of nanothermites in advanced technologies.

References

[1] Ji Young Ahn, Ji Hoon Kim, Jong Man Kim, Deug Woo Lee, Jong Kweon Park, Donggeun Lee, and Soo Hyung Kim. Combustion characteristics of high-energy Al/CuO composite powders: The role of oxidizer structure and pellet density. *Powder Technology*, 241:67–73, 2013.

[2] Ji Young Ahn, Sang Beom Kim, Ji Hoon Kim, Nam Su Jang, Dae Hyun Kim, Hyung Woo Lee, Jong Man Kim, and Soo Hyung Kim. A micro-chip initiator with controlled combustion reactivity realized by integrating Al/CuO nanothermite composites on a microhotplate platform. *Journal of Micromechanics and Microengineering*, 26(1):015002, 2015.

[3] Mehdi Bahrami, Guillaume Taton, Véronique Conédéra, Ludovic Salvagnac, Christophe Tenailleau, Pierre Alphonse, and Carole Rossi. Magnetron sputtered Al/CuO nanolaminates: Effect of stoichiometry and layers thickness on energy release and burning rate. *Propellants, Explosives, Pyrotechnics*, 39(3):365–373, 2014.

[4] Vincent Baijot, Djafari-Rouhani Mehdi, Carole Rossi, and Alain Estève. A multi-phase micro-kinetic model for simulating aluminum based thermite reactions. *Combustion and Flame*, 180:10–19, 2017.

[5] Jeffrey M Bergthorson. Recyclable metal fuels for clean and compact zero-carbon power. *Progress in Energy and Combustion Science*, 68:169–196, 2018.

[6] Malcolm W Chase. NIST-JANAF thermochemical tables 4^{th} edition. *Journal of Physical and Chemical Reffernce Data*, pages 1529–1564, 1998.

[7] Y-K Chen and Frank S Milos. Ablation and thermal response program for spacecraft heatshield analysis. *Journal of Spacecraft and Rockets*, 36(3):475–483, 1999.

[8] Snehaunshu Chowdhury, Kyle Sullivan, Nicholas Piekiel, Lei Zhou, and Michael R Zachariah. Diffusive vs explosive reaction at the nanoscale. *The Journal of Physical Chemistry C*, 114(20):9191–9195, 2010.

[9] John A Dec, Robert D Braun, and Bernard Laub. Ablative thermal response analysis using the finite element method. *Journal of Thermophysics and Heat Transfer*, 26(2):201–212, 2012.

[10] Luigi T DeLuca. Overview of Al-based nanoenergetic ingredients for solid rocket propulsion. *Defence Technology*, 14(5):357–365, 2018.

[11] David MB Dombroski, Anqi Wang, John Z Wen, and Marco Alfano. Joining and welding with a nanothermite and exothermic bonding using reactive multi-nanolayers–a review. *Journal of Manufacturing Processes*, 75:280–300, 2022.

[12] Garth C Egan, Edward J Mily, Jon-Paul Maria, and Michael R Zachariah. Probing the reaction dynamics of thermite nanolaminates. *The Journal of Physical Chemistry C*, 119(35):20401–20408, 2015.

[13] Garth C Egan and Michael R Zachariah. Commentary on the heat transfer mechanisms controlling propagation in nanothermites. *Combustion and Flame*, 162(7):2959–2961, 2015.

[14] Joseph Mark Epps, Jean-Pierre Hickey, and John Z Wen. Modelling reaction propagation for Al/CuO nanothermite pellet combustion. *Combustion and Flame*, 229:111374, 2021.

[15] Mark E Ewing, Travis S Laker, and David T Walker. Numerical modeling of ablation heat transfer. *Journal of Thermophysics and Heat Transfer*, 27(4):615–632, 2013.

[16] S Fischer and Mark Grubelich. A survey of combustible metals, thermites, and intermetallics for pyrotechnic applications. In *32nd Joint Propulsion Conference and Exhibit*, page 3018, 1996.

[17] S Fischer and Mark Grubelich. Theoretical energy release of thermites, intermetallics, and combustible metals. Technical report, Sandia National Lab. (SNL-NM), Albuquerque, NM (United States), 1998.

[18] Christopher Greenshields. *OpenFOAM v10 User Guide*. The OpenFOAM Foundation, London, UK, 2022.

[19] Fabien Halter, Samuel Jeanjean, Christian Chauveau, Youssef Berro, Marianne Balat-Pichelin, Jean-François Brilhac, Adeline Andrieu, Cornelius Schonnenbeck, Gontrand Leyssens, and Clément Dumand. Recyclable metal fuels as future zero-carbon energy carrier. *Applications in Energy and Combustion Science*, 13:100100, 2023.

[20] Rohit J Jacob, Kevin J Hill, Yong Yang, Michelle L Pantoya, and Michael R Zachariah. Pre-stressing aluminum nanoparticles as a strategy to enhance reactivity of nanothermite composites. *Combustion and Flame*, 205:33–40, 2019.

[21] Shruti Kabra, Swaroop Gharde, Prakash M Gore, Sunil Jain, Vrushali H Khire, and Balasubramanian Kandasubramanian. Recent trends in nanothermites: Fabrication, characteristics and applications. *Nano Express*, 1(3):032001, 2020.

[22] Maasoud Kaviany. *Principles of heat transfer in porous media*. Springer Science & Business Media, 2012.

[23] Kyoungjin Kim. Computational modeling of combustion wave in nanoscale thermite reaction. *International Journal of Energy and Power Engineering*, 8(7):679–682, 2014.

[24] Suyong Kim and Sili Deng. Inference of chemical kinetics and thermodynamic properties from constant-volume combustion of energetic materials. *Chemical Engineering Journal*, page 143779, 2023.

[25] Suyong Kim, Averitt A Johns, John Z Wen, and Sili Deng. Burning structures and propagation mechanisms of nanothermites. *Proceedings of the Combustion Institute*, 39(3):3593–3604, 2023.

[26] Jean Lachaud. PATO: Porous-material Analysis Toolbox. https://pato.ac/, 2025. Accessed: 2025-01-14.

[27] Jean Lachaud, Nagi Mansour, Alejandro Ceballos, Dusan Pejakovic, Luning Zhang, and Jochen Marschall. Validation of a volume-averaged fiber-scale model for the oxidation of a carbon-fiber preform. In 42^{nd} *AIAA Thermophysics Conference*, page 3640, 2011.

[28] Jean Lachaud and Nagi N Mansour. Porous-material analysis toolbox based on OpenFOAM and applications. *Journal of Thermophysics and Heat Transfer*, 28(2):191–202, 2014.

[29] Jean Lachaud, James B Scoggins, Thierry E Magin, MG Meyer, and Nagi N Mansour. A generic local thermal equilibrium model for porous reactive materials submitted to high temperatures. *International Journal of Heat and Mass Transfer*, 108:1406–1417, 2017.

[30] Jean Lachaud, Tom van Eekelen, James B Scoggins, Thierry E Magin, and Nagi N Mansour. Detailed chemical equilibrium model for porous ablative materials. *International Journal of Heat and Mass Transfer*, 90:1034–1045, 2015.

[31] Nagi N Mansour, Francesco Panerai, Jean Lachaud, and Thierry Magin. Flow mechanics in ablative thermal protection systems. *Annual Review of Fluid Mechanics*, 56(1):549–575, 2024.

[32] Jeremie BE Meurisse, Jean Lachaud, Francesco Panerai, Chun Tang, and Nagi N Mansour. Multidimensional material response simulations of a full-scale tiled ablative heatshield. *Aerospace Science and Technology*, 76:497–511, 2018.

[33] I Monk, M Schoenitz, RJ Jacob, EL Dreizin, and MR Zachariah. Combustion characteristics of stoichiometric Al/CuO nanocomposite thermites prepared by different methods. *Combustion Science and Technology*, 189(3):555–574, 2017.

[34] Maurizio Natali, Jose Maria Kenny, and Luigi Torre. Science and technology of polymeric ablative materials for thermal protection systems and propulsion devices: A review. *Progress in Materials Science*, 84:192–275, 2016.

[35] Turkuler Ozgumus, Moghtada Mobedi, and Unver Ozkol. Determination of Kozeny constant based on porosity and pore to throat size ratio in porous medium with rectangular rods. *Engineering Applications of Computational Fluid Mechanics*, 8(2):308–318, 2014.

[36] Won Chan Park, Arvind Atreya, and Howard R Baum. Experimental and theoretical investigation of heat and mass transfer processes during wood pyrolysis. *Combustion and flame*, 157(3):481–494, 2010.

[37] Yajing Peng, Yinghui Wang, Bruno Palpant, Xing He, Xianxu Zheng, and Yanqiang Yang. Modeling heat-induced chemical reaction in nanothermites excited by pulse laser: A hot spot model. *International Journal of Modern Physics B*, 24(03):381–395, 2010.

[38] Jan Puszynski, Chris J Bulian, and Jacek J Swiatkiewicz. Ignition characteristics of nanothermite systems. *International Journal of Energetic Materials and Chemical Propulsion*, 7(1), 2008.

[39] Thomas Rogaume. Thermal decomposition and pyrolysis of solid fuels: Objectives, challenges and modelling. *Fire Safety Journal*, 106:177–188, 2019.

[40] Florin Saceleanu, Mahmoud Idir, Nabiha Chaumeix, and John Z Wen. Combustion characteristics of physically mixed 40 *nm* aluminum/copper oxide nanothermites using laser ignition. *Frontiers in Chemistry*, 6:465, 2018.

[41] James B Scoggins, Vincent Leroy, Georgios Bellas-Chatzigeorgis, Bruno Dias, and Thierry E Magin. Mutation++: Multicomponent thermodynamic and transport properties for ionized gases in C++. *SoftwareX*, 12:100575, 2020.

[42] James B Scoggins and Thierry E Magin. Gibbs function continuation for linearly constrained multiphase equilibria. *Combustion and Flame*, 162(12):4514–4522, 2015.

[43] Dilip Sundaram, Vigor Yang, and Richard A Yetter. Metal-based nanoenergetic materials: Synthesis, properties, and applications. *Progress in Energy and Combustion Science*, 61:293–365, 2017.

[44] Rajagopalan Thiruvengadathan. Aluminum-based nano-energetic materials: State of the art and future perspectives. *Nano-energetic materials*, pages 9–35, 2019.

[45] Rajagopalan Thiruvengadathan and Anqi Wang. Nanoenergetic materials: From materials to applications. *Nanomaterials*, 14(19):1574, 2024.

[46] Emelian Tichtchenko, Alain Estève, and Carole Rossi. Modeling the self-propagation reaction in heterogeneous and dense media: Application to Al/CuO thermite. *Combustion and Flame*, 228:173–183, 2021.

[47] Emelian Tichtchenko, V Folliet, Olivier Simonin, Benoît Bédat, L Glavier, Alain Estève, and Carole Rossi. Combustion model for thermite materials integrating explicit and coupled treatment of condensed and gas phase kinetics. *Proceedings of the Combustion Institute*, 39(3):3637–3645, 2023.

[48] Emilian Tichtchenko, Benoît Bédat, Olivier Simonin, Ludovic Glavier, David Gauchard, Alain Estève, and Carole Rossi. Comprehending the influence of the

particle size and stoichiometry on Al/CuO thermite combustion in close bomb: A theoretical study. *Propellants, Explosives, Pyrotechnics*, page e202200334, 2023.

[49] Henk A Van der Vorst. Bi-CGSTAB: A fast and smoothly converging variant of Bi-CG for the solution of nonsymmetric linear systems. *SIAM Journal on Scientific and Statistical Computing*, 13(2):631–644, 1992.

[50] Haiyang Wang, Dylan J Kline, and Michael R Zachariah. In-operando high-speed microscopy and thermometry of reaction propagation and sintering in a nanocomposite. *Nature Communications*, 10(1):3032, 2019.

[51] Moran Wang and Ning Pan. Predictions of effective physical properties of complex multiphase materials. *Materials Science and Engineering: R: Reports*, 63(1):1–30, 2008.

[52] Xiangwen Wang, Zhirong Wang, Lei Ni, Ming Zhu, and Chuipeng Liu. Explosion characteristics of aluminum powder in different mixed gas environments. *Powder technology*, 369:53–71, 2020.

[53] MR Weismiller, JY Malchi, RA Yetter, and TJ Foley. Dependence of flame propagation on pressure and pressurizing gas for an Al/CuO nanoscale thermite. *Proceedings of the Combustion Institute*, 32(2):1895–1903, 2009.

[54] Tao Wu, Guillaume Lahiner, Christophe Tenailleau, Benjamin Reig, Teresa Hungría, Alain Estève, and Carole Rossi. Unexpected enhanced reactivity of aluminized nanothermites by accelerated aging. *Chemical Engineering Journal*, 418:129432, 2021.

[55] Yu-Shu Wu, Karsten Pruess, and Peter Persoff. Gas flow in porous media with Klinkenberg effects. *Transport in Porous Media*, 32:117–137, 1998.

[56] Mohamed Gaber Zaky, Ahmed Elbeih, and Tamer Elshenawy. Review of nanothermites: A pathway to enhanced energetic materials. *Central European Journal of Energetic Materials*, 18(1), 2021.

[57] James Zapata, Andrea Nicollet, Baptiste Julien, Guillaume Lahiner, Alain Estève, and Carole Rossi. Self-propagating combustion of sputter-deposited Al/CuO nanolaminates. *Combustion and Flame*, 205:389–396, 2019.

[58] Yiqi Zhang, Hongtao Sui, Yuning Li, and John Z Wen. Energetic characteristics of the Al/CuO core-shell composite micro-particles fabricated as spherical colloids. *Thermochimica Acta*, 689:178656, 2020.

APPENDICES

Appendix A

Detailed Analysis of the Bprime Boundary Condition

This appendix presents a detailed examination of the chemical equilibrium within the boundary control volume under the Bprime boundary condition, emphasizing the formation reactions of species and the thermodynamic principles governing equilibrium [28].

The formation reaction of species A_i within the control volume can be expressed as the equilibrium between the species and its constituent elements, as follows:

$$A_i \rightleftharpoons \sum_{k \in Elements} \nu_{i,k} A_k \tag{A.1}$$

The thermodynamics of i chemical equilibria is described as follows:

$$\sum_{k \in Elements} \nu_{i,k} \ln(x_k) - \ln(x_i) - \ln(\mathcal{K}_i) = 0 \tag{A.2}$$

where $\mathcal{K}_i$ is the equilibrium constant associated with the formation reaction of species A_i, The value of $\mathcal{K}_i$ is available in the Mutation^{++} database and is determined based on the quasi-steady temperature and pressure within the control volume. The sum of species mole fraction (x_i) is equal to one:

$$\sum_{i \in Species} x_i = 1 \tag{A.3}$$

The set of provided equations, along with the conservation of element mass fractions in the control volume, yields the unknowns $\dot{m}_{ca}$, $z_{i,w}$:

$$\rho_e u_e C_H \left(z_{i,w} - z_{i,e}\right) + (\dot{m}_{pg} + \dot{m}_{ca}) z_{i,w} = \dot{m}_{pg} z_{i,pg} + \dot{m}_{ca} z_{i,ca} \tag{A.4}$$

These formulations are the quasi-steady chemical equilibrium equations provided by the Mutation^{++} library and implemented in PATO as the Bprime boundary condition. The base model can be expanded as necessary to include multicomponent mass transfer, unequal diffusion coefficients, failure mechanisms such as spallation and melting, a solid phase composed of multiple elements, and heterogeneous finite-rate chemical reactions.